

# Waves in waterways generated by moving pressure field in Boussinesq equations using unstructured finite element model

S. Agarwal<sup>a</sup>, V. Sriram<sup>a,\*</sup>, P. L.-F. Liu<sup>a,b,c</sup>, K. Murali<sup>a</sup>

<sup>a</sup>Department of Ocean Engineering, Indian Institute of Technology Madras, India

<sup>b</sup>Department of Civil and Environmental Engineering, National University of Singapore, Singapore

<sup>c</sup>Department of Hydraulic and Ocean Engineering, National Cheng Kung University, Tainan, Taiwan

---

## Abstract

A finite element model for depth integrated form of Boussinesq equations is presented. The equations are solved on an unstructured triangular mesh using standard Galerkin method with mixed interpolation scheme. The elemental integrals are calculated analytically and time-stepping is done using Runge-Kutta 4<sup>th</sup> order method. It is extended to simulate ship-generated waves using moving pressure fields. The unstructured formulation provides the flexibility of mesh refinement as needed, for capturing wave transformation or moving pressure field. The model is verified against experimental and numerical results for wave transformation over the Whalin shoal. The results for moving pressure field are compared against numerical results from FUNWAVE. Further, a simulation of ship navigating a curved path is presented. Finally, a real-life application and validation against field measurements is provided for waves generated by a fast ferry moving along a GPS tracked path in Tallinn Bay, Estonia.

Manuscript accepted in Ocean Engineering

Published version at <https://doi.org/10.1016/j.oceaneng.2022.112202>

Cite as :

Agarwal, S., Sriram, V., Liu, P. L.-F., Murali, K. (2022). Waves in waterways generated by moving pressure field in Boussinesq equations using unstructured finite element model. *Ocean Engineering*, 262, 112202, ISSN 0029-8018.

[doi:10.1016/j.oceaneng.2022.112202](https://doi.org/10.1016/j.oceaneng.2022.112202)

© 2022 This manuscript version is made available under the CC-BY-NC-ND 4.0 

**Keywords:** Boussinesq-type equations, Finite element method, Unstructured grid, Ship generated waves, Moving surface pressure, Waterways and port engineering

---

## 1. Introduction

Coastal and ocean engineering problems involve a wide range of temporal and spatial scales. These vary from long tsunami waves to steep deep-water waves to breaking waves in the surf zone. The objective of modelling the propagation and transformation of this wide range of waves over large domains with variable bathymetry has led to the development of two-dimensional horizontal (2DH) models. They capture the three-dimensional physics on a two-dimensional scale, thus offering improved computational efficiency compared to the fully-resolved three-dimensional models, without a significant loss in accuracy.

The range of applicability of 2DH models is mainly categorised based on the non-linearity parameter  $\epsilon = a/h$  and dispersion parameter  $\mu = h/L$ . Here  $h$  is the still-water depth,  $L$  is the characteristic wave-length and  $a$  is the wave-amplitude. The

classic Boussinesq-type equations [1] were developed using perturbation method in depth-integrated form assuming irrotational flow, weak non-linearity and weak dispersion. Therefore, these are valid for small amplitude waves in shallow depths up-to  $kh \approx 1$ , with  $O(\mu^2) = O(\epsilon) \ll 1$ . Here  $k = 2\pi/L$  is the wave-number. The dispersion characteristics of these equations were improved using long-wave equation, resulting in the Madsen and Sørensen's form [2] and the Beji's form [3] of Boussinesq equations. Similarly, the Nwogu's form [4] improved the dispersion characteristics by evaluating velocity at a tuned z-level of  $z_\alpha = -0.531h$  from mean sea-level. These modified forms are weakly non-linear and weakly dispersive, with extended validity till intermediate depths up-to  $kh \approx 3$  for small amplitude waves. By taking  $O(\epsilon) = 1$  and retaining the  $O(\mu^2)$  terms, highly non-linear but weakly dispersive Liu [5] and Wei [6] form of the equations were developed for modelling steeper waves up-to  $kh \approx 3$ . The highly non-linear forms have improved shoaling characteristics in the surf zone. It was reported in [6] that the weakly non-linear forms result in over-prediction of shoaling as the wave approaches

---

\*Corresponding author

Email address: [vsriram@iitm.ac.in](mailto:vsriram@iitm.ac.in) (V. Sriram )

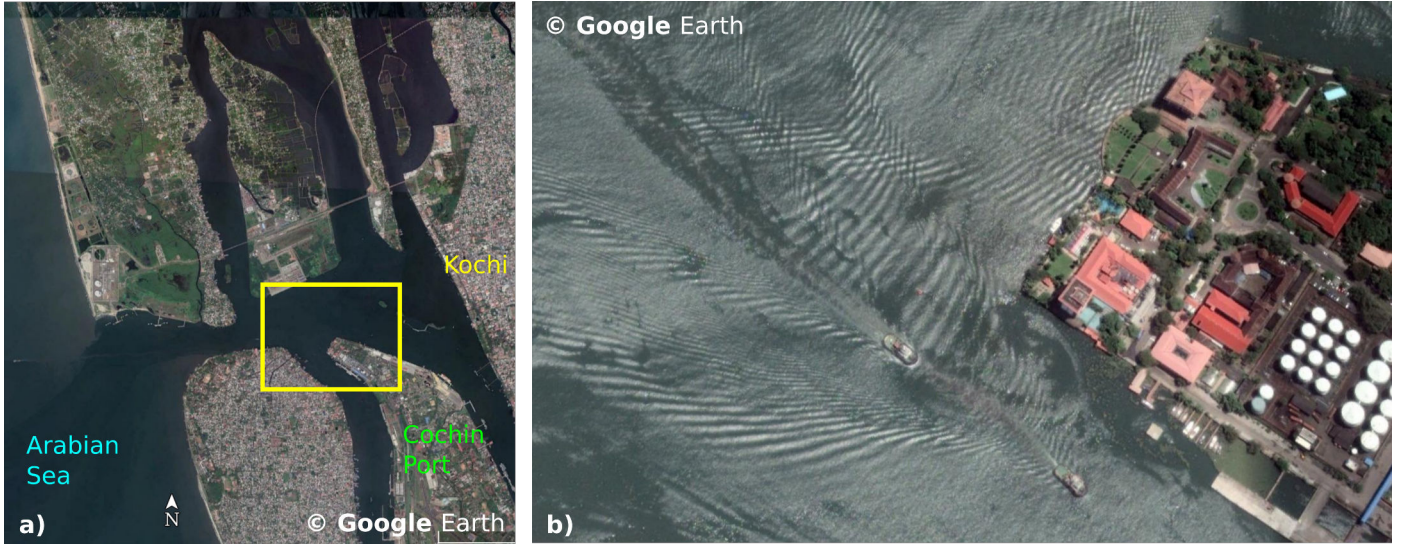


Figure 1: a) The natural harbour of Cochin port in India, that is accessed by large vessels through the Arabian sea. b) Satellite image of the highlighted section obtained from Google Earth located at 9.97° N, 76.25° E, dated August-2015, displaying a section of the Cochin port in Kochi, India. It shows the interaction of waves generated by two vessels and their combined impact on the shoreline.

the breaking point. However, this was updated in the study by [7] which investigated various weakly-nonlinear Boussinesq equations in amplitude-velocity and amplitude- volume flux forms. It concluded that when approaching non-linear regimes, the amplitude-velocity forms result in over-prediction, while amplitude-volume flux forms result in marginal under-prediction of shoaling. Liu's form of the equations was developed into a general purpose model COULWAVE [8, 9] using finite-difference method (FDM). Similarly the Wei's form was developed into a widely used FDM-FVM model named FUNWAVE-TVD [10]. The work in [11] presented a higher order model by retaining  $O(\mu^4)$  terms and using a linear combination of velocities at two arbitrary z-levels. This form demonstrated improved dispersion characteristics till  $kh \approx 6$ , and also provides vertical distribution of velocity accurate up-to  $kh \approx 4$ . However, the formulation includes higher than third order spatial derivatives, thus requiring additional boundary conditions and complex numerical implementation. A comprehensive review of Boussinesq equations is presented in [12], where the defining physics, and the mathematical and numerical techniques involved in development of the various forms is discussed. In contrast to the aforementioned forms, the Green-Naghdi equations [13] are 2DH equations which were developed using the theory of directed fluid sheets, similar to nonlinear plate theory. The Korteweg-de Vries (KdV) equation [14] is a nonlinear dispersive single variable reduction of the classic Boussinesq equations which can be solved analytically [15, 16, 17]. Other forms of 2DH equations include, multi-layer methods were developed which divide the water column into multiple layers and match the pressures and horizontal velocities at the interface [18, 19]. This approach can simulate steeper waves in deeper water, but with more number of governing equations due to the use of multiple layers. More recently a wave-current 2DH model derived using weighted residual method, applicable till deep water was presented in [20],

with further development for arbitrary current profiles in [21].

Apart from wind generated waves, Boussinesq-type equations can be used for modelling waves generated by moving vessels. In high traffic regions, the long-period waves generated by ships can propagate over large distances and impact the surrounding coastline. Further, in areas such as harbours or bays, ship-generated waves may have a significant impact, especially if these regions are protected from wind-generated waves due to the presence of landmasses or breakwaters. Fig. (1) shows one such example of the natural harbour of Cochin port in southern India. The port is located on an artificial island in the brackish waters of the local backwaters, and therefore is protected from the ocean by the surrounding features as shown in Fig. (1a). Due to this, the waves generated by vessels approaching the commercial port or the naval port have a heavy impact on the densely populated coastline. A similar example of Tallinn Bay in Estonia is discussed in section 4.5, where a field study was conducted to identify the regions which are sensitive to the long-waves generated by fast moving ferries [22]. Worldwide, such scenarios can be seen in heavy traffic regions such as approach channels, harbours and inland waterways.

Boussinesq-type models can be used for studying these large domain problems, with the effect of the moving ship implemented either through moving pressure field or a flux source. The flux source method was used in [23] for generating the ship wake in rectangular and trapezoidal channels. The work in [24] further developed the approach by correcting the errors in the conservation of mass arising from asymmetric bow and stern shape. The more commonly used approach of moving pressure field also was used for studying ship wakes in various channels using FUNWAVE-TVD [25], COULWAVE [26] and several other models [27, 28]. Further the non-linearity in interaction between wakes of two vessels was investigated using FUNWAVE-TVD in [29], with advanced results for breaking solitons separating ahead of the moving disturbance presented

in [30]. The generation of solitons ahead of vessels moving in narrow channels was also studied in [31] using the Green-Naghdi equations. Simulations in relatively unrestricted domain were done using COULWAVE in [32, 33] for studying the spatial variation of ship-generated waves for high speed vessels over the uneven bathymetry of Tallinn bay in Estonia. The inclusion of porosity as done in [34, 35] for simulating porous breakwaters can further enhance the functionality.

It should be noted that the majority of simulations of ship-generated waves in the mentioned literature were done on structured grids. The versatility of Boussinesq-type equations can lead to multiple length scales in a simulation of large domain. These may range from long waves in deeper depths to very short waves in the shallow depths. Further a shorter length scale may be required for capturing a vessel's shape for simulating ship-generated waves. The mesh size in a structured grid is limited by the shortest length scale. This may lead to a computationally inefficient situation, where long waves are being captured by small mesh size. This large ratio of characteristic wave-length to mesh size will require a small time-step for computational stability and hence further reducing the efficiency. Alternatively, an unstructured grid can provide the required flexibility in mesh sizing and can also capture boundaries with complex geometries.

The finite-element method (FEM) has been applied on unstructured grids to solve various forms of the Boussinesq equations. Initial developments include the work done by [36] which solved the classic form [1] using linear triangular elements and the Taylor-Galerkin method. Further FEM models were developed on extended Boussinesq equations [2, 3, 4] for application in intermediate depths. These models often include auxiliary governing equations for resolving the third order spatial derivatives in the extended forms. The work in [37] modelled the Nwogu's form [4] using linear triangular elements, two auxiliary equations for the higher order terms and a adaptive time-stepping procedure based on backward-differentiation method. They reported presence of high-frequency oscillations in the results which are smoothed using a tuned fourth-order viscous term in the free-surface equation. The work in [38] solved the Beji's form [3] using linear rectangular elements, used the gradient of surface-elevation as the auxiliary variable and employed a high-order predictor-corrector time-marching algorithm. This work too reports high-frequency oscillations in the results, especially in the beginning of a wave-train, which are treated using a time-ramping approach. The numerical oscillations in these models are likely due to the use of equal-order shape function for surface-elevation and velocities, as argued in [39]. Therefore, the model in [39] employs a mixed formulation with linear elements for surface-elevation and quadratic element for the velocities. This model uses a single auxiliary equation for the second derivation of surface-elevation and uses an explicit three-step time-stepping method for efficient computation. The work in [40] avoided use of auxiliary variable by using a cubic weight function and a linear shape function in a Petrov-Galerkin FEM formulation for 1D Nwogu's form of the equations. However, the procedure was found to be difficult to reproduce in 2D. Therefore, their two-dimensional FEM model

for Nwogu's form in [41] used a Galerkin formulation with linear triangular elements, predictor-corrector time-stepping and employed two auxiliary governing equations with emphasis on the treatment of no-flux boundary. Alternatively, the discontinuous Galerkin FEM (DG-FEM) scheme has also been applied for solving Boussinesq equations on unstructured grids. This scheme does not require the solution to be continuous across element boundaries. Therefore, it is especially useful in Boussinesq equations involving high order derivatives. Similar to the finite-volume methods, this scheme requires additional calculation of inter-element flux. The work in [42] models the weakly non-linear Madsen form [43] using the DG-FEM scheme using a slope limiter scheme for inter-element flux calculation. The model in [44] solves the fully non-linear Madsen form [45] using DG-FEM and employs the Lax-Friedrich scheme for the inter-element fluxes.

There is a lack of numerical results from unstructured FEM models for ship-generated waves, especially given their strength in capturing multiple length scales. The paper presents a finite-element model for Madsen and Sørensen's form of Boussinesq equation [43], with emphasis on simulating wave generated by moving vessels. We follow the mixed formulation approach of [39] and use the standard Galerkin method with mixed linear and quadratic shape functions. Further, instead of using the standard Gaussian quadrature method, we calculate the elemental integrals analytically. Unlike the Taylor-Galerkin approach in [39], we use the Runge-Kutta 4<sup>th</sup> order time-stepping method and evaluate the two momentum equations together. This avoid the requirement of iterating the solution for achieving convergence. We implement the moving pressure field approach for simulating ship-generated waves and further validate this through field results. The paper briefly presents the governing equations in section 2, followed by the development details of this finite element model named FEBOUSS in section 3. The following sections present various numerical results presenting the validation and application of the model. Section 4.2 presents validation against experimental and numerical results for combined wave refraction and diffraction over the Whalin shoal [46]. The results for waves generated by ship moving along a straight line are compared against numerical results from FUNWAVE-TVD in section 4.3. We further simulate a ship navigating a curved channel to identify the simulation requirements for the curved path of a moving pressure field in section 4.4. Building upon these results, the final section 4.5 presents a real-life application and validation against field measurements for waves generated by a fast ferry moving along a GPS tracked path in Tallinn Bay, Estonia.

## 2. Governing Equations

This work uses Madsen and Sørensen's depth integrated form of Boussinesq equation for slowly varying bathymetry presented in [43]. Assuming incompressible, inviscid and irrotational flow, the equations are first derived using perturbation method in [1], with improvements in dispersion characteristics presented in [2]. It was shown to have excellent agreement for

shoaling coefficient and phase celerity for waves till intermediate depth region  $kh \approx 3$  in [43], thus enabling its application in near-shore regions where the effects of sea-bottom are present. The continuity equation and the depth integrated X and Y momentum equation are given as follows:

$$\frac{\partial \eta}{\partial t} + \frac{\partial P}{\partial x} + \frac{\partial Q}{\partial y} = 0, \quad (1a)$$

$$\begin{aligned} \frac{\partial P}{\partial t} + \frac{\partial}{\partial x} \left( \frac{P^2}{d} \right) + \frac{\partial}{\partial y} \left( \frac{PQ}{d} \right) + gd \frac{\partial \eta}{\partial x} \\ + \Psi_1 + \frac{\tau_1}{\rho} + \frac{d}{\rho} \frac{\partial \Pi}{\partial x} = 0, \end{aligned} \quad (1b)$$

$$\begin{aligned} \frac{\partial Q}{\partial t} + \frac{\partial}{\partial x} \left( \frac{PQ}{d} \right) + \frac{\partial}{\partial y} \left( \frac{Q^2}{d} \right) + gd \frac{\partial \eta}{\partial y} \\ + \Psi_2 + \frac{\tau_2}{\rho} + \frac{d}{\rho} \frac{\partial \Pi}{\partial y} = 0. \end{aligned} \quad (1c)$$

Here  $g$  is the acceleration due to gravity,  $\rho$  is the density of water,  $\eta$  is the instantaneous free surface elevation,  $h$  is the still-water depth,  $d = h + \eta$  is the instantaneous total water depth and  $P$  and  $Q$  are depth integrated velocities along the X and Y axes respectively, i.e.,  $P = \int_{-h}^{\eta} u dz$ . The values  $P$  and  $Q$  may also be referred to as volume-flux [7]. The additional Boussinesq terms  $\Psi_1$  and  $\Psi_2$  are responsible for the dispersion characteristics of the model and have the following forms:

$$\begin{aligned} \Psi_1 = - (B + \frac{1}{3})h^2(P_{xxt} + Q_{xyt}) - hh_x(\frac{1}{3}P_{xt} + \frac{1}{6}Q_{yt}) \\ - \frac{1}{6}hh_yQ_{xt} - Bgh^3(\eta_{xxx} + \eta_{xyy}) \\ - Bgh^2h_x(2\eta_{xx} + \eta_{yy}) - Bgh^2h_y\eta_{xy}, \end{aligned} \quad (2a)$$

$$\begin{aligned} \Psi_2 = - (B + \frac{1}{3})h^2(P_{xyt} + Q_{yyt}) - hh_y(\frac{1}{6}P_{xt} + \frac{1}{3}Q_{yt}) \\ - \frac{1}{6}hh_xP_{yt} - Bgh^3(\eta_{xxy} + \eta_{yyy}) \\ - Bgh^2h_y(\eta_{xx} + 2\eta_{yy}) - Bgh^2h_x\eta_{xy}. \end{aligned} \quad (2b)$$

Here the subscripts denote partial derivatives, i.e.,  $P_{xxt} = \frac{\partial}{\partial t} \left( \frac{\partial P}{\partial x} \right)$ . The terms  $(\tau_1, \tau_2)$  in Eqs. (1b) and (1c) correspond to the shear stress arising from the boundary layer along the bottom boundary. They are estimated using quadratic friction law as follows [47]:

$$(\tau_1, \tau_2) = \rho C_b \frac{\sqrt{P^2 + Q^2}}{d^2} (P, Q), \quad (3)$$

where  $C_b$  is the bottom drag coefficient based on Manning coefficient. The final terms in Eqs. (1b) and (1c) are gradient of surface pressure  $\Pi$ . They are used for implementing a moving pressure field to simulate ship-generated waves. This procedure is discussed in detail in the following sections.

The governing equation in this form involves up to 3rd-order spatial derivatives of surface elevation. A high order polynomial shape function would be needed for  $\eta$  to model those

terms. In order to eliminate these terms [39] introduced an auxiliary variable  $\omega$  as

$$\omega = \frac{\partial}{\partial x} \left( h \frac{\partial \eta}{\partial x} \right) + \frac{\partial}{\partial y} \left( h \frac{\partial \eta}{\partial y} \right). \quad (4)$$

Therefore, the auxiliary variable equation is a part of the governing equations along with the conservation of mass and momentum. The corresponding Boussinesq terms become:

$$\begin{aligned} \Psi_1 = - (B + \frac{1}{3})h^2(P_{x^2t} + Q_{xyt}) - hh_x(\frac{1}{3}P_{xt} + \frac{1}{6}Q_{yt}) \\ - \frac{1}{6}hh_yQ_{xt} - Bgh^2\omega_x, \end{aligned} \quad (5a)$$

$$\begin{aligned} \Psi_2 = - (B + \frac{1}{3})h^2(P_{xyt} + Q_{y^2t}) - hh_y(\frac{1}{6}P_{xt} + \frac{1}{3}Q_{yt}) \\ - \frac{1}{6}hh_xP_{yt} - Bgh^2\omega_y. \end{aligned} \quad (5b)$$

Here  $B$  is the free parameter for tuning the dispersion characteristics. Through comparisons of wave celerity against Stokes first order theory, the value of  $B = 1/15$  was found to have less than 5% error till intermediate water  $kh \approx 3$  in [2], with further validations in [43] using linear shoaling analysis.

The present work does not include additional terms corresponding to wave breaking and eddy-viscosity based turbulence as the analysis is limited to non-breaking cases.

## 2.1. Moving pressure field

Models based on Boussinesq equations have been used for simulating waves generated by moving vessels. However, with the depth dimension either integrated or averaged in these models, it would not be possible to simulate near-vessel flow. Therefore, the effect of a vessel moving through the waters is implemented in Boussinesq equations either by approximating near-vessel flow using slender-body theory [23, 24]; or by adding pressure source terms to the conservation of momentum equations [27, 28, 31].

The slender-body approach calculates the flux generated in the direction perpendicular to the motion of the vessel using the variation of its transverse section area. This transverse section area can be estimated analytically [24], but can also be calculated numerically for any vessel shape. Changing the direction of motion of a vessel may lead to complications because it would need calculation of transverse and longitudinal section area. Additional modifications would be needed to avoid errors in conservation of mass arising from the difference in flux generated by the bow and stern regions, as discussed in [24]. Given that the approach relies on the gradient of sectional area, a transom stern will be difficult to achieve due to the abrupt gradient.

The present work uses moving pressure field to generate the waves from moving vessels. A surface pressure term  $\Pi$  is added to momentum equations as shown in Eq. (1). Here  $\Pi(x, y, t) = \rho g D(x, y, t)$  is defined as hydrostatic pressure due to the local draft  $D(x, y, t)$  of the vessel at time  $t$ . The shape of the vessel can be given either through analytical forms or through discrete points. However, structures, which are submerged or are flaring inwards, cannot be included in this approach. This

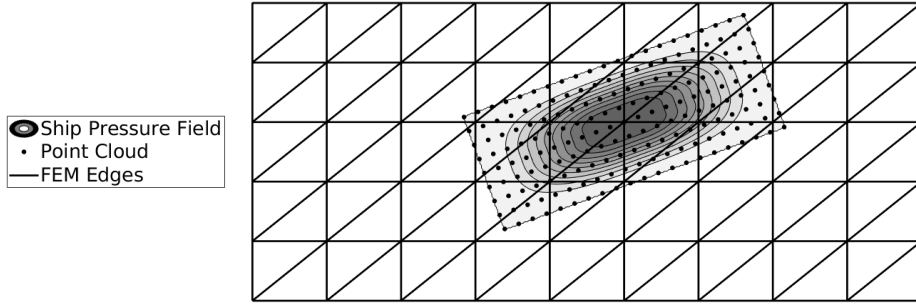


Figure 2: Schematic showing the point cloud over the vessel's pressure field, which is used for estimating the wave-making forces on the vessel using moving least squares method.

approach can neither model a transom stern due to the sharp gradient of hydrostatic pressure. Consider a ship with length  $L_s$ , beam  $B_s$ , draft  $D_s$ , centre  $(x_s(t), y_s(t))$  and heading  $\theta_s(t)$  with respect to positive X-axis at time  $t$ . In the existing literature on wave generated by moving pressure field in Boussinesq models, the draft function  $D(x, y, t)$  is often prescribed using one of two analytical expressions. The first expression as defined in [31] is given as follows:

$$D(x, y, t) = D_s f(x') g(y'), \quad (6a)$$

$$f(x') = \begin{cases} \cos^2 \left[ \pi \left( \frac{x' - 0.5\alpha_1}{1 - \alpha_1} \right) \right] & 0.5\alpha_1 < x' \leq 0.5 \\ \cos^2 \left[ \pi \left( \frac{x' + 0.5\alpha_2}{\alpha_2 - 1} \right) \right] & -0.5 \leq x' < -0.5\alpha_2 \\ 1 & -0.5\alpha_2 \leq x' \leq 0.5\alpha_1 \end{cases} \quad (6b)$$

$$g(y') = \begin{cases} \cos^2 \left[ \pi \left( \frac{y' - 0.5\beta_1}{1 - \beta_1} \right) \right] & 0.5\beta_1 < y' \leq 0.5 \\ \cos^2 \left[ \pi \left( \frac{y' + 0.5\beta_1}{\beta_1 - 1} \right) \right] & -0.5 \leq y' < -0.5\beta_1 \\ 1 & -0.5\beta_1 \leq y' \leq 0.5\beta_1 \end{cases} \quad (6c)$$

where

$$\begin{pmatrix} x' \\ y' \end{pmatrix} = \begin{bmatrix} \frac{1}{L_s} & 0 \\ 0 & \frac{1}{B_s} \end{bmatrix} \begin{bmatrix} \cos(\theta_s(t)) & \sin(\theta_s(t)) \\ -\sin(\theta_s(t)) & \cos(\theta_s(t)) \end{bmatrix} \begin{pmatrix} x - x_s(t) \\ y - y_s(t) \end{pmatrix}. \quad (7)$$

There are 3 controlling coefficients;  $\alpha_1, \alpha_2 \in [0, 1]$  for shaping the bow and stern parts, and  $\beta_1 \in [0, 1]$  for the transverse cross-section. This expression allows for both slender and bulky pressure fields. The second expression as defined in [27, 28] is given as follows:

$$D(x, y, t) = D_s \left[ 1 - \alpha_1(x')^4 \right] \left[ 1 - \beta_1(y')^2 \right] \exp \left[ -\beta_2(y')^2 \right], \quad (8)$$

$$-0.5 \leq x' \leq 0.5, -0.5 \leq y' \leq 0.5$$

It results in a slender ship with only the keel at maximum draft. The coefficient  $\alpha_1$  in Eq. (8) controls the longitudinal shape, while  $\beta_1$  and  $\beta_2$  shape the transverse cross-section. However, with typical values of  $\alpha_1 = 16$  and  $\beta_1 = 4$ , this expression offers limited control over the pressure field's shape. The coefficients in both of these expressions are used to modify the shape of the pressure field to match the physical loaded displacement of the ship.

The vessel is moved simply by moving the centre of the pressure field  $(x_s(t), y_s(t))$  and changing the heading  $\theta_s(t)$  over time as required. Therefore, it can perform oblique or rotatory motions. In order to follow an arbitrary path, the position and heading should be given by the user at multiple time-instances. The actual path at simulation time-step is interpolated between user specified positions using cubic spline method. The significance of this is briefly discussed in section 4.4. Further, we can simulate multiple vessels by adding the pressure term due to each vessel to the governing equation.

### 3. Numerical Formulation

The system of governing equations, with the auxiliary variable given by Eq. (4), continuity and momentum equation by Eq. (1), are solved in space using finite element method. The problem domain  $\Omega$ , with the boundary  $\Gamma$ , is divided into non-overlapping irregular triangles, thus generating an unstructured mesh. This allows for capturing of complex boundaries. We use the standard Galerkin method, where the same polynomial is used as basis and test functions. Given the presence of up-to second order spatial derivatives for  $\eta$ ,  $P$  and  $Q$ , a minimum of  $C^0$  continuous basis function will be needed with the use of integration by parts. However, as argued in [39], use of equal order basis functions for velocities and surface elevation will lead to spurious oscillations. Therefore a mixed formulation is used, with the stable form for triangular element as suggested in [48]. The variables  $\eta$  and  $\omega$  are evaluated at the 3 vertices of the triangle using linear basis function  $\psi$ . The variables  $P$  and  $Q$  are evaluated at the 3 vertices and the 3 edge-centres of the triangle, using the quadratic basis function  $\phi$ . Hence collectively throughout the domain, there will be  $N_l$  nodes where  $\eta$  and  $\omega$  are evaluated, and  $N_q$  nodes where  $P$  and  $Q$  are evaluated. The values of the unknowns within a triangular element are given in the following forms.

$$P(x, y) = \sum_{i=1}^6 \phi_i P_i, \quad Q(x, y) = \sum_{i=1}^6 \phi_i Q_i. \quad (9a)$$

$$\eta(x, y) = \sum_{i=1}^3 \psi_i \eta_i, \quad \omega(x, y) = \sum_{i=1}^3 \psi_i \omega_i. \quad (9b)$$

The weak form of the governing equations is obtained by multiplying Eq. (4) and Eq. (1a) with  $\psi$ , and multiplying

Eq. (1b) and Eq. (1c) with  $\phi$ , and then integrating over the element. The integration is carried out by parts when necessary, resulting in boundary integrals and reduction of the order of the derivatives. The derivatives inside an element are evaluated using Jacobian and coordinate transformation to master element. Instead of using the traditional numerical approach of Gauss quadrature for evaluating the elemental integrals, we calculate the integrated expression analytically using symbolic maths in Mathematica [49] and code it directly into the program. This will reduce the computational effort, especially for large domains. The procedure is described in detail in [Appendix A](#).

The time marching in this model is done using the classic Runge-Kutta 4<sup>th</sup> order scheme (RK4), with a prescribed constant time-step. Therefore, the system would have to be solved 4 times per time-step, making it computationally expensive compared to explicit approaches such as Adam-Bashforth 3rd order scheme. However, its low local truncation error of  $O(\Delta t^5)$  allows for larger time-step and lower accumulation of error over long simulation duration. With the use of RK4, the algebraic system of time derivatives  $\dot{\eta}$ ,  $\dot{P}$  and  $\dot{Q}$  is formed as presented in Eq. (10).

$$\begin{bmatrix} M_2 \end{bmatrix} \omega = \begin{bmatrix} D \end{bmatrix} \eta, \quad (10a)$$

$$\begin{bmatrix} M_2 \end{bmatrix} \dot{\eta} = \begin{bmatrix} C_x \end{bmatrix} P + \begin{bmatrix} C_y \end{bmatrix} Q - \begin{bmatrix} \chi M_2 \end{bmatrix} \eta, \quad (10b)$$

$$\begin{aligned} & \begin{bmatrix} M_1 + B_1 & B_2 \\ B_3 & M_1 + B_4 \end{bmatrix} \begin{pmatrix} \dot{P} \\ \dot{Q} \end{pmatrix} \\ &= \begin{bmatrix} N & 0 \\ 0 & N \end{bmatrix} \begin{pmatrix} P \\ Q \end{pmatrix} + \begin{bmatrix} G_x \\ G_y \end{bmatrix} \eta + \begin{bmatrix} B_5 \\ B_6 \end{bmatrix} \omega \\ &+ \begin{bmatrix} E_x \\ E_y \end{bmatrix} \Pi - \begin{bmatrix} \chi M_1 & 0 \\ 0 & \chi M_1 \end{bmatrix} \begin{pmatrix} P \\ Q \end{pmatrix}. \end{aligned} \quad (10c)$$

The system is solved in the sequence as shown in Eq. (10) during each step of RK4. The matrices on the LHS are the global stiffness matrix for each system. For  $\omega$  and  $\dot{\eta}$ , the stiffness matrix  $[M_2]$  is square with a size of  $(N_l \times N_l)$ .  $\dot{P}$  and  $\dot{Q}$  are solved together due to their interdependence, making their stiffness matrix of size  $(2N_q \times 2N_q)$ . The expressions on RHS are written in global matrix form for fast computation. Few of the matrices on the RHS are constant and are evaluated once at the beginning of the simulation. These are multiplied with the dynamic values of the unknowns to obtain the RHS of the system of linear equations. Expressions for all matrices are included in [Appendix B](#).

The constant time-step for the simulation is prescribed based on Courant number condition

$$Cou = \max\left\{\frac{\Delta t}{\Delta r}, \sqrt{gh}\right\}. \quad (11)$$

Usually  $Cou \leq 1$  is a sufficient condition for a stable simulation. Here  $h$  and  $\Delta r$  are the local water-depth and characteristic mesh dimension respectively. The dispersion error for

this mixed linear-quadratic scheme is reported in [Appendix C](#), similar to the analysis for various schemes conducted in [50]. All of the matrices in Eq. (10) are sparse, and are stored using compressed sparse row (CSR) technique, which converts the two-dimensional matrix into two one dimensional matrix with information of only the non-zero values. This drastically reduces storage requirement and improves access speed. The system of linear equations can be solved using direct methods, such as Gaussian elimination. However, the numerical implementation of these methods require significantly high memory and computation, making them viable only for small problems. Alternatively, iterative methods such as the bi-conjugate gradient stabilised method (BiCGStab) employed in this work, allow for efficient solution of large-domain problems. However, the iterative solvers require a terminating criterion, which is specified as absolute tolerance of  $10^{-4}$  for the presented system based on numerical tests.

### 3.1. Boundary Conditions

Three boundary conditions (BC) have been implemented in the current model, including inlet, wall and absorbing boundaries. The inlet is implemented using Dirichlet BC, where values of  $P$ ,  $Q$  and  $\eta$  at inlet boundary nodes are either given using analytical theories such as Airy wave theory and Stokes 2<sup>nd</sup> order theory, or evaluated using Fourier series solution for the Boussinesq equations at constant depth as presented in [51]. Alternatively, we can also provide input from a fully-nonlinear potential theory (FNPT) model. The wall boundary condition is implemented using  $P_n = Pn_x + Qn_y = 0$  for slip-wall, where  $(n_x, n_y)$  is outward unit normal, and  $P = 0$ ,  $Q = 0$  for no-slip wall. The absorbing boundary is implemented using a sponge layer based on Newtonian cooling [52]. It is applied to continuity and momentum equations, with additional  $-\chi\eta$ ,  $-\chi P$  and  $-\chi Q$  terms on the RHS of the respective governing equations, Eq. (10b-10c). Here  $\chi$  is a ramping function defined as

$$\chi(x) = \frac{30 \exp\left(\frac{x-x_a}{L_a}\right)^2 - 1}{T_a \exp(1) - 1}, \quad 0 < (x - x_a) < L_a, \quad (12)$$

where  $T_a$  is time period of wave to be absorbed,  $L_a$  is the length of the sponge layer and  $x_a$  represents the coordinate for the beginning of the sponge layer. This expression is modified appropriately for sponge layer along other directions. The use of this ramping function along with proper length of the sponge layer is crucial for minimising reflection of the wave from the sponge layer.

### 3.2. Wave-making force on pressure field

Wave-making forces on the moving pressure field in Boussinesq model were estimated in the work of [31] by using hydrostatic pressure and gradient of surface elevation as

$$(F_x, F_y) = \iint_{\Omega_s} \rho g D \left( \frac{\partial \eta}{\partial x}, \frac{\partial \eta}{\partial y} \right) dx dy. \quad (13)$$

In the present work, a regularly spaced point cloud, as shown in Fig. (2), is attached to the rectangular region of the moving

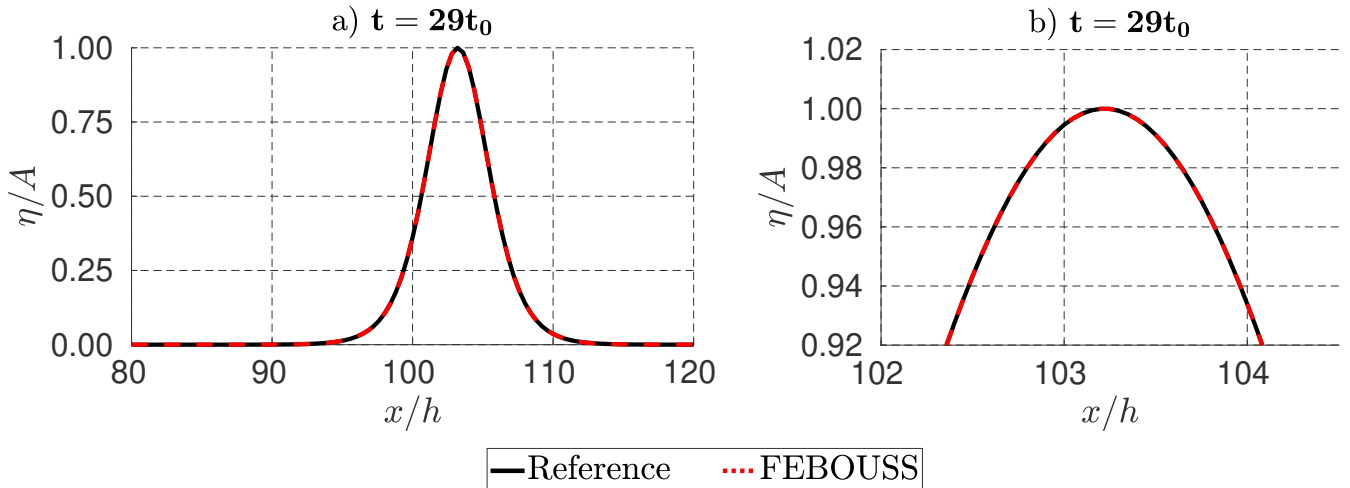


Figure 3: Surface-elevation plot of solitary wave at  $t = 29t_0$  obtained by FEBOUSS simulation using  $\Delta x = 0.05h$  mesh-resolution compared against solution to Eq. (15) as the reference. a) Zoomed-out view, b) Zoomed-in of the peak.

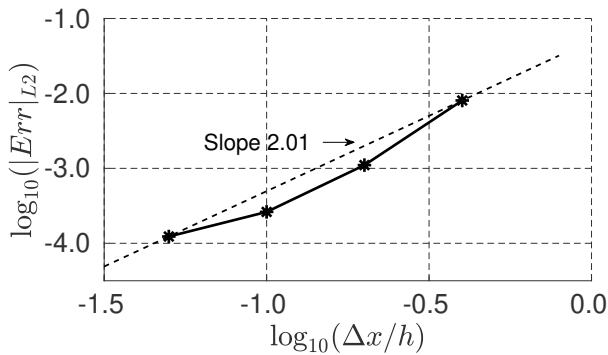


Figure 4: Plot of L2 norm of error in surface-elevation profile for various mesh resolutions. The dashed line has a slope of 2.01, indicating a nearly quadratic rate of convergence.

pressure field. The values of hydrostatic pressure and  $\nabla\eta$  are evaluated at these points. This allows for accurate calculation of Eq. (13) for multiple pressure fields while they move along arbitrary paths.

Due to the  $C^0$  continuous  $\eta$  across FEM elements,  $\nabla\eta$  obtained from FEM shape function at the nodes of the point-cloud will be discontinuous across each element. Therefore, we instead use the moving least squares method (MLS) [53] to obtain continuous  $\nabla\eta$  at the nodes of the point-cloud. Finally, due to the regular distribution of the nodes in the point-cloud, the area integral in Eq. (13) is conveniently calculated using Simpson's rule.

Viscous and wave-making forces are two major components of the resistance for a vessel moving in calm water. For vessels moving in shallow water, both of these forces are increased due to the faster motion of water under the vessel, and higher amplitudes of the generated waves. An accurate numerical calculation of these forces would require intensive three-dimensional viscous flow simulations. We would like to acknowledge that the wave-making resistance obtained from Eq. (13) is only in-

dicative. Additionally, this derived quantity can be used for monitoring the flow and simulation convergence in the vicinity of the pressure field. The obtained forces may indicate the trend of wave-making resistance while the pressure field moves over variable bathymetry and is explored in section 4.5. However, the correlation between this estimation and actual wave-making resistance is beyond the scope of this manuscript.

#### 4. Numerical Results

The section presents convergence analysis, validation and numerical results for this unstructured finite element model for Boussinesq equation (FEBOUSS). The mesh convergence is studied using solitary wave propagation and the standard test case of Whalin shoal [46]. Further results are presented for waves generated by moving pressure fields.

##### 4.1. Solitary wave propagation and mesh convergence

Consider a solitary wave of amplitude  $A$  in a one-dimensional domain with constant still-water depth  $h$ . The solitary wave will have a self-similar solution, i.e,

$$\eta(x, t) = \eta(\xi) \quad P(x, t) = P(\xi) \quad \text{where} \quad \xi = x - Ct \quad (14)$$

Here,  $C$  is the celerity of the solitary wave. Further, assuming that the solution and all its derivatives tend to zero as  $\xi \rightarrow \pm\infty$ , the one-dimensional form of the Boussinesq equations Eq. (1) can be reduced to a second-order ordinary differential equation for  $P$ , given by

$$\begin{aligned} \frac{\partial^2 P}{\partial \xi^2} & \left( \frac{Bgh^3}{C} - Ch^2 \left( B + \frac{1}{3} \right) \right) \\ & = \left( \frac{gh - C^2}{C} \right) P + \left( \frac{g}{2C^2} \right) P^2 + \frac{CP^2}{Ch + P} \end{aligned} \quad (15)$$

$$\text{where, } C^2 = \frac{ghA^2(A + 3h)}{6h^2(A - h \ln(1 + \frac{A}{h}))}$$

The surface-elevation is obtained by  $\eta(\xi) = P(\xi)/C$ . The derivation of this procedure is described in [54]. This ordinary differential equation can be numerically solved, with boundary condition  $P(0) = CA$  and  $\frac{\partial}{\partial \xi}P(0) = 0$ , to obtain a relatively 'exact' solution for the solitary wave. This solution is provided as the initial condition in FEBOUSS to simulate solitary waves.

A mesh convergence analysis was conducted using a solitary wave with  $A/h = 0.2$  in water depth  $h = 1\text{m}$ . The resultant celerity from Eq. (15) is  $C = 3.4407\text{m/sec}$ . The length scale is non-dimensionalised using  $h$  and the time-scale using  $t_0 = \frac{h}{C}$ . Each simulation was done on a rectangular numerical domain consisting of regularly spaced nodes, with  $\Delta x = \Delta y$ , length  $300h$  spanning between  $x \in [-100h, 200h]$  and width  $10\Delta x$ . The slip-wall condition is applied at all four boundaries. Tests were conducted for  $\Delta x \in \{0.40h, 0.20h, 0.10h, 0.05h\}$ . The Courant number for each simulation was fixed at  $Cou = 0.43$ , resulting in time-step  $\Delta t/t_0 = 0.43\frac{\Delta x}{h}$ . The initial condition was specified using the solution to Eq. (15), with the peak located at  $x = 0h$  at  $t = 0t_0$ .

The solitary wave profile obtained from FEBOUSS at  $t = 29t_0$  after about  $100h$  distance of propagation is compared with the solution to Eq. (15) as the reference. Fig. (3) presents a nearly overlapping comparison of the surface elevation obtained using  $\Delta x = 0.05h$  against the reference. The mesh resolution will impact the profile and celerity of the solitary wave. At  $t = 29t_0$ , we quantify the error using the L2 norm of relative difference between the simulated  $\eta_F$  and reference  $\eta_{ref}$  profiles,  $Err = \frac{\|\eta_F - \eta_{ref}\|_2}{A}$ . Fig. (4) presents the plot of the error against the mesh-resolution. The slope of this plot indicates the rate of convergence of the model. The dashed line in Fig. (4) has a slope of 2.01, indicating an overall quadratic rate of convergence. This analysis thus validates the convergence and accuracy of the FEBOUSS simulation for the basic test case of solitary wave propagation.

#### 4.2. Regular waves over Whalin shoal

An experimental investigation for combined refraction diffraction was carried out by [46]. They used a shoaling bathymetry with parallel circular contours, which were symmetric about the centreline of the rectangular basin. The trials were limited to non-breaking cases, and the wave generation at the beginning of the basin was linear. Therefore, these experiments present a good test case for investigation of non-linear refraction and diffraction modelled by this FEM model FEBOUSS. The bathymetry setup for the experiments is given by

$$h(x, y) = \begin{cases} 0.4572 & 0 \leq x \leq 10.67 - G \\ 0.4572 + \frac{1}{25}(10.67 - G - x) & 10.67 - G \leq x \leq 18.29 - G \\ 0.1524 & 18.29 - G \leq x \leq 36.576 \end{cases} \quad (16a)$$

$$G(y) = \sqrt{(y(6.096 - y))} \quad 0 \leq y \leq 6.096, \quad (16b)$$

with maximum and minimum depth of  $h_1 = 0.4572\text{m}$  and  $h_2 = 0.1524\text{m}$  respectively. A contour plot for this bathymetry

is shown in Fig. (5a). In the original work [46], a number of experiments were conducted on the same bathymetry for various wave periods, 1s, 2s and 3s, with the waves generated at the deeper end of  $h_1 = 0.4572\text{m}$ . We have presented results for two cases, case-1 with  $T = 1\text{s}$ ,  $H = 0.039\text{m}$ ,  $kh_1 = 1.92$ ; and case-2 with  $T = 2\text{s}$ ,  $H = 0.015\text{m}$ ,  $kh_1 = 0.73$ . Numerical tests for these experiments were also carried out by [43] using a FDM model, and [39] using a FEM model for similar governing equations.

We first present the results for case-2 with  $T = 2\text{s}$ . The domain is rectangular with dimensions  $36.576\text{m} \times 6.096\text{m}$ . For these tests a regular mesh consisting of right-angled isosceles triangles with sides  $\Delta x = \Delta y$  is considered. The waves are generated on the left boundary using analytical expression from Stokes 2<sup>nd</sup> order theory. A sponge layer of length  $L_a = 6.576\text{m}$ , starting at  $x_a = 30\text{m}$  is placed on the right boundary. The remaining boundaries are slip walls. With this setup the simulation soon reaches a steady state.

We conduct a self-convergence study for the model using mesh setups shown in Table (1). Here  $L_1 = 3.909\text{m}$  and  $L_2 = 2.382\text{m}$  are the wave-lengths obtained from linear dispersion relationship for the  $T = 2\text{s}$  wave at the deepest and the shallowest depths of  $h_1 = 0.4572\text{m}$  and  $h_2 = 0.1524\text{m}$  respectively. As per the recommendations in [2], 8–10 grid points are sufficient to capture a regular wave. This is taken as the coarsest setup M1 in our study. The Courant number defined by Eq. (11) is kept around  $Cou = 0.85$  for all setups. The resultant wave elevation obtained using various mesh setups along the domain's centreline at  $y = 3.048\text{m}$  is shown in Fig. (6). It presents visual representation of the mesh convergence through the overlapping results of M5 and M6. The self-convergence is further quantified using error parameter  $P_d = \sqrt{\sum(\eta - \eta_{ref})^2 / \sum(\eta_{ref})^2}$  [55], where  $P_d \rightarrow 0$  indicates perfect agreement between the two signals. We compare the results from M1–M5 against the reference setup M6 using  $P_d$  in Fig. (8a). We observe limited change in results beyond M4 setup.

We also investigate the time-step convergence for this model. The setup M3 with spacing  $0.2032\text{m}$  was simulated with time-steps  $\Delta t = [0.08, 0.05, 0.04, 0.03125, 0.025]$  corresponding to  $T/\Delta t = [25, 40, 50, 64, 80]$  respectively, covering Courant number range from  $0.26 – 0.84$ . We placed three wave-probes along the domain's centreline at  $y = 3.048\text{m}$ ; WP1 in the region of wave-generation at  $x = 5\text{m}$ , WP2 in the middle of the shoal at  $x = 12\text{m}$ , and WP3 in the post shoaling wave-peak region at  $x = 20\text{m}$ . Fig. (7) presents the wave-elevation time-series at WP3 ( $x, y$ ) = (20, 3.048)m for various time-steps. We observed limited difference in results for time-steps smaller than  $T/40$ . The error parameter  $P_d$  is evaluated for wave-elevation time series for various time-steps. Here the time-series from the smallest time-step  $\Delta t = T/80$  is taken as the reference. Fig. (8b) shows the plot of error  $P_d$  at each of the three wave-probe locations. The value of  $P_d$  is close to zero for all test cases, however we can still observe a significant reduction in  $P_d$  for the wave probe at  $x = 20\text{m}$ . This is likely due to the introduction of higher harmonics in this region, which will be discussed further in this section. From these analyses we can observe the mesh and time-step convergence for this FEM model of the

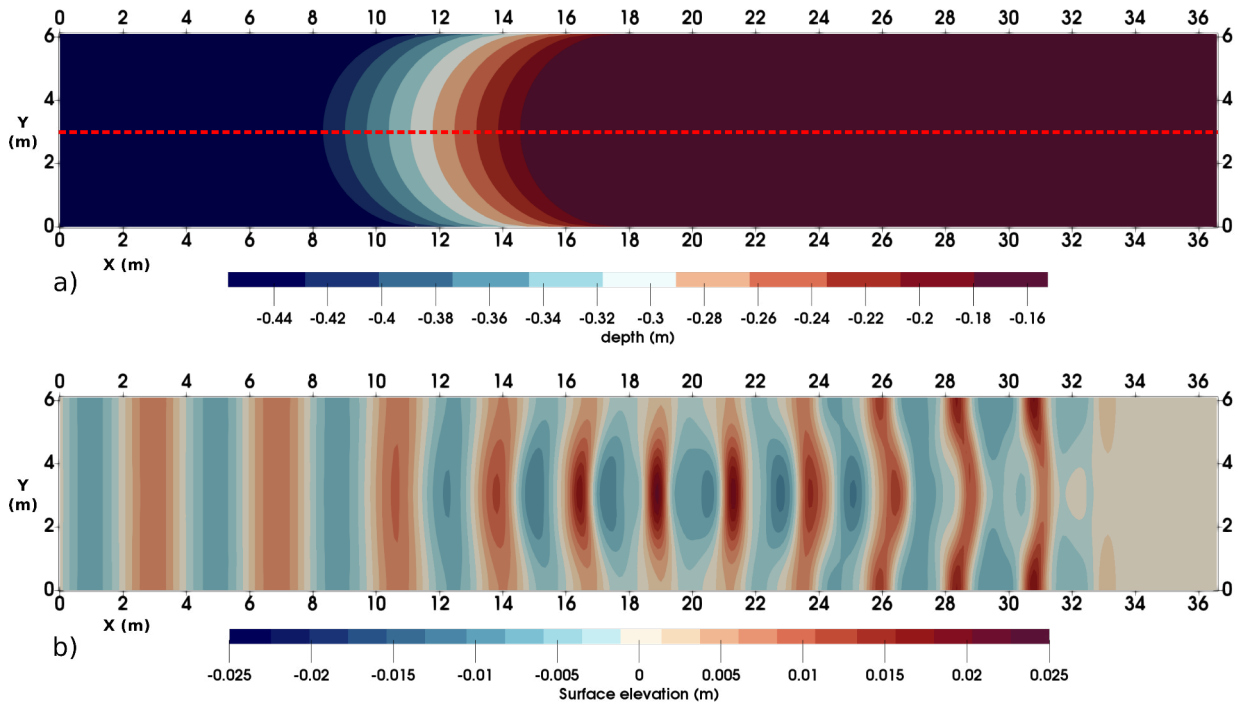


Figure 5: a) Contour plot showing the bathymetry for Whalin shoal [46] test cases. The dashed line depicts the domain's centreline at  $y = 3.048\text{m}$ , along which measurements are reported in Fig. (6,9,10,11). b) Numerical result for contour of wave elevation at  $t = 40\text{s}$  for case-2.

Table 1: Details of the simulation setups for the convergence study for regular wave of  $T = 2\text{s}$ ,  $H = 0.015\text{m}$  transforming over Whalin shoal's bathymetry. Here the Courant number is kept within  $0.83 - 0.87$  for all setups.

Setup	$\Delta x = \Delta y$ (m)	$L_1/\Delta x$	$L_2/\Delta x$	$\Delta t$ (s)	$T/\Delta t$	Courant	Number of elements
M1	0.3048	12.83	7.82	0.125	16	0.87	4,800
M2	0.2540	15.40	9.38	0.10	20	0.83	6,912
M3	0.2032	19.24	11.73	0.08	25	0.83	10,800
M4	0.1524	25.65	15.63	0.0625	32	0.87	19,200
M5	0.1016	38.48	23.45	0.04	50	0.83	43,200
M6	0.0762	51.30	31.27	0.03125	64	0.87	76,800

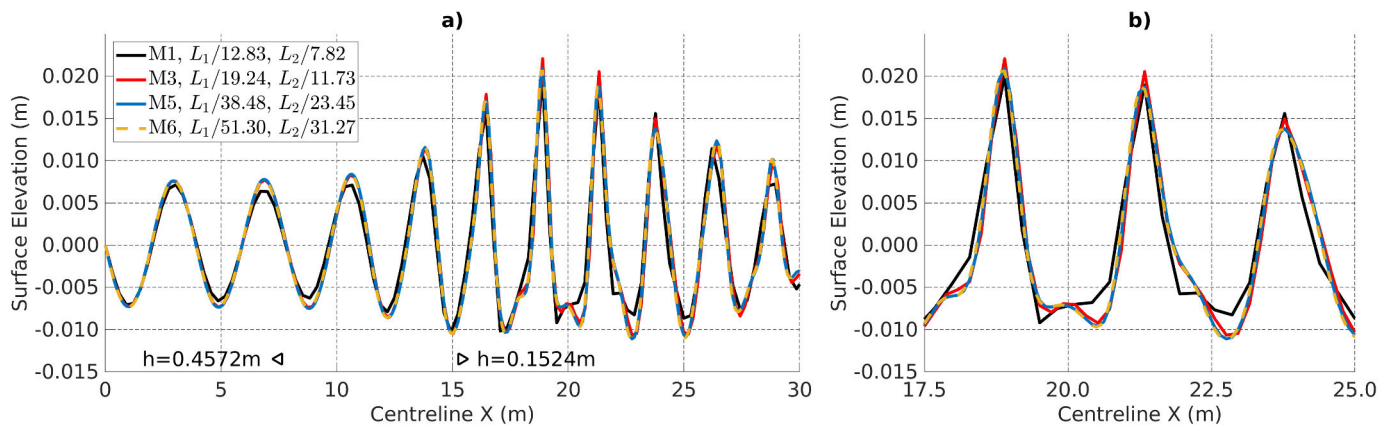


Figure 6: Wave elevation along the domain centreline  $y = 3.048\text{m}$  at  $t = 40\text{s}$  for case-2 obtained using mesh setups M1, M3, M5, M6 from Table (1). a) Zoomed out view from wave generation to wave transformation. b) Zoomed in view near the peak elevation region. Please note the legend is common for plots a) and b).

Boussinesq equations. For this particular test case, a mesh size of  $L/16$ , where  $L$  is the shortest wave-length, and time-step of  $T/40$  is a sufficient resolution. However these guidelines will vary depending on the steepness of the waves.

The converged results obtained using the setup M5 will be used for further analysis. It corresponds to 43200 triangular elements with 22021 and 87241 nodes for linear and quadratic interpolation respectively. The contour plot of wave-elevation in Fig. (5b) shows the regular waves transform over the shoal and refracting towards the centreline. The wave-elevation along the centreline shows good agreement against previous numerical results from [39] in Fig. (9). Due to the non-linear wave transformation over the shoal, energy gets transferred to higher harmonics. This is observed through Fig. (10b) showing non-zero amplitude around 0.5Hz, 1.0Hz, 1.5Hz corresponding to first, second and third harmonics. The experiments by [46] had measured amplitudes of the first, second and third harmonics. A comparison between these amplitudes from experimental results of [46], numerical results of Taylor-Galerkin FEM model in [39], numerical results of DG-FEM model in [44] and our simulations is shown in Fig. (10a). When compared with [39], our model provides comparable results for the same mesh size with 4 times the time-step. This is due to the RK4 time-stepping and also because we solve the interdependent governing equations for  $P$  and  $Q$  together, as shown in Eq. (10c), instead of the iteration procedure used by [39].

The second test was conducted for case-1 with  $T = 1\text{s}$ . For this case we obtained converged results for the same domain with mesh size of 0.0508m and time-step  $\Delta t = 0.02\text{s}$ . This shorter and steeper wave after transformation shows transfer of energy mainly to the second harmonic. This is seen in the non-zero amplitudes for 1.0Hz and 2.0Hz corresponding to the first and the second harmonics in Fig. (11b). The amplitudes of first and second harmonic along the centreline are compared in Fig. (11a) against the experiments, the FDM results with  $B = 1/15$  from [43] and the hybrid FDM-FVM model from [56]. Our results also include the amplitude for the third harmonic. The FDM results have oscillations in the amplitude of the second harmonic, but the same was not observed in our results. Although the experiments have considerable scatter for this case even before the shoaling event, our results show good agreement for the first harmonics and slight under-estimation for the second harmonic amplitudes.

We have also investigation mass conservation properties of the FEM model. A control volume is taken between  $x = 6.096\text{m}$  and  $x = 29.464\text{m}$ , which is bound by the walls along the Y-axis, and the bathymetry and the free surface along the Z-axis. The error in conservation of mass within this control volume is given by  $E = \frac{d}{dt} \left( \int_{CV} \rho dV \right) + \int_{CS} \rho (\vec{v}_r \cdot \vec{n}) dS$  [57, Eq. (3.20)]. Here  $CV$  and  $CS$  are the control volume and the corresponding control surface,  $\vec{n}$  is outward unit normal for the control surface and  $\vec{v}_r$  is the relative velocity between the fluid and the control surface. The error is non-dimensionalised using mass flux under the wave crest during wave-generation  $E_{nd}$ , which is calculated analytically from Stokes 2<sup>nd</sup> order theory. This represents the conservation error with respect to the wave input into the control volume. This error is calculated at each

time-step during the simulation and is reported for both case-1 and case-2 in Fig. (12). We observe that for both cases, the error in mass conservation over the entire computational domain is within 5% of the wave crest's mass flux throughout the simulation period. However higher error is observed in the steeper case-1 due to the weakly non-linear nature of the Boussinesq equation. Through these numerical results we have demonstrated the performance of FEBOUSS for combined non-linear refraction diffraction problems against other models for similar equations and against experiments.

#### 4.3. Waves generated by moving pressure field

In this section we present results for waves generated by a pressure field moving in straight line. When floating bodies move in calm water, the generated wake is referred to as Kelvin wave pattern. It consists of transverse waves, which move behind the vessel and divergent waves, which move outward from the moving disturbance. In finite depth, the dominance of transverse and divergent systems and the subsequent Kelvin pattern is dependant upon depth Froude number  $Fr_d = \frac{V_s}{\sqrt{gh}}$ , where  $V_s$  is the ship speed and  $h$  is the still water-depth. The transition between these two systems is a system of wave cusps which move along with the vessel [58]. The angle made by the cusps with the path of the vessel is called the half-wedge angle  $\theta_K$ . The work in [58] provides analytical expression for the half wedge angle  $\theta_K$  and the wave-length at cusps  $L_H$  for a point impulse moving in calm water at a given  $Fr_d$ .

We present a study similar to the work in [28], where a FDM-FVM model called BOSZ based on Nwogu's form of Boussinesq equation was used to simulate waves generated by vessels of various sizes with analytical shape given by Eq. (8). The work in [27] conducted similar trials using a staggered C-grid FDM model for the weakly non-linear weakly dispersive Beji's form [3] of the equations, where they presented results for the wedge angle for various Froude numbers for a vessel with shape given by Eq. (8). We have presented our results in comparison with similar simulations done using FUNWAVE-TVD.

The domain is rectangular with dimensions  $840\text{m} \times 408\text{m}$ , with a constant still-water depth of  $h = 5\text{m}$ . The vessel has length  $L_s = 36\text{m}$ , beam  $B_s = 6\text{m}$ , draft  $D_s = 1\text{m}$ . Its shape is defined by Eq.(8), with coefficients  $\alpha_1 = 16$ ,  $\beta_1 = 2$  and  $\beta_2 = 16$ . The ship characteristics are similar to tests done in [28]. The vessel is moved without acceleration in initially calm water, with the ship centre starting at  $(51.0\text{m}, 204.0\text{m})$  and moving along the X-axis at a constant velocity of  $5.95\text{m s}^{-1}$ , corresponding to a depth Froude number  $Fr_d = 0.85$ . A sponge layer of  $30\text{m}$  is placed on each of the 4 boundaries to absorb the vessel wake. The wave elevation is monitored along various sections that run along the length of the domain as shown in Fig. (13). Additionally two probes P1 and P2 are placed at mirrored location about the centreline along with another probe P3 to report temporal measurements.

The mesh size for vessel wake simulations will be dependant on the wave-lengths in the wave group and the size of the vessel. We consider the wave-length at cusps  $L_H$  and the width of the vessel  $B_s = 6$  as the defining parameters. For  $Fr_d = 0.85$ ,

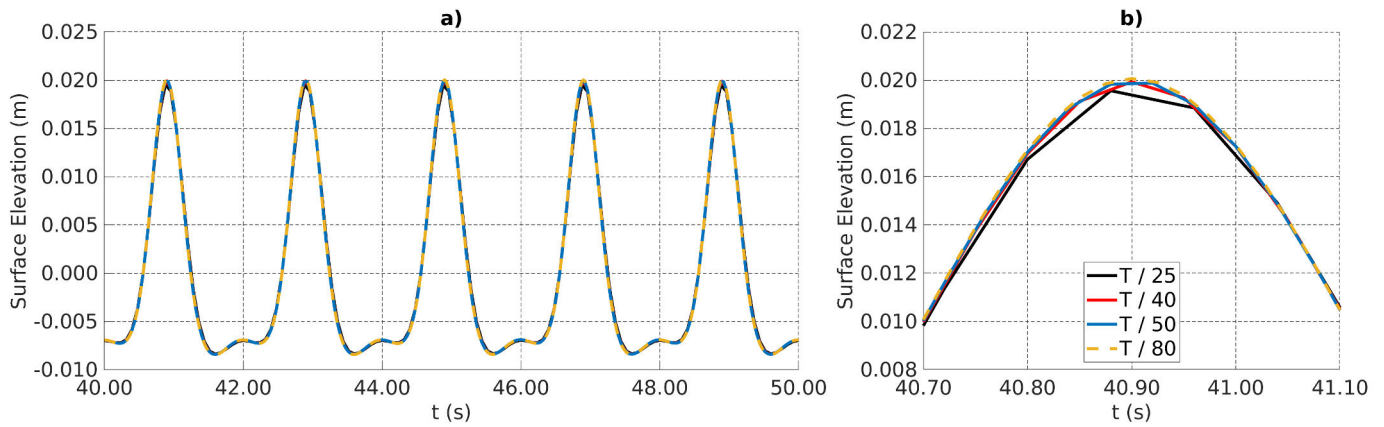


Figure 7: a) Numerical wave elevation measured at post shoaling peak elevation wave-probe ( $x, y$ ) = (20, 3.048)m for various simulation time-steps with mesh size  $\Delta x = \Delta y = 0.2032\text{m}$ . b) Zoomed in view of the crest of wave elevation measured at ( $x, y$ ) = (20, 3.048)m for various simulation time-steps with mesh size  $\Delta x = \Delta y = 0.2032\text{m}$ , highlighting the influence of simulation time-step. Please note the legend is common for plots a) and b).

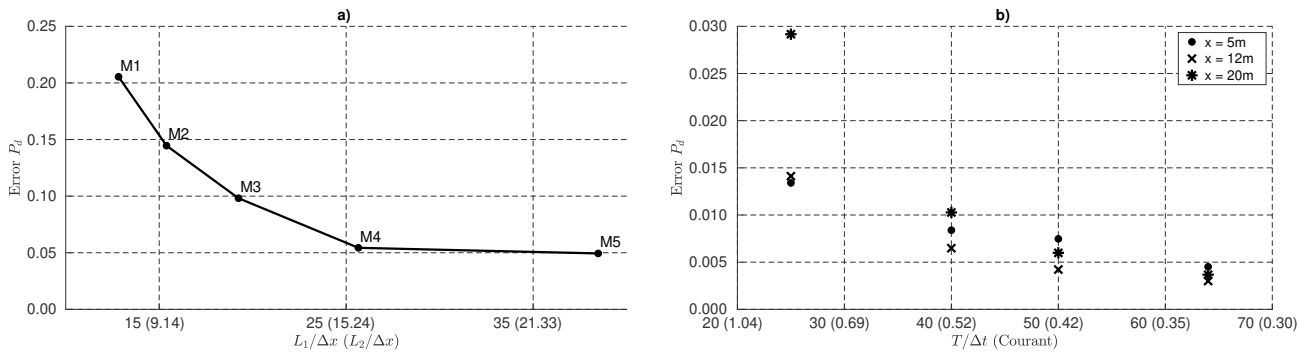


Figure 8: a) Plot showing quantification of self-convergence through error parameter  $P_d$  obtained from setups M1-M5 compared against setup M6. b) Plot demonstrating the time-step convergence using wave-elevations measured at wave-probes located at  $(x, y)$  = (5, 3.048)m,  $(x, y)$  = (12, 3.048)m and  $(x, y)$  = (20, 3.048)m. The error  $P_d$  is evaluated for various time-steps, with  $\Delta t = T/80$  as the reference.

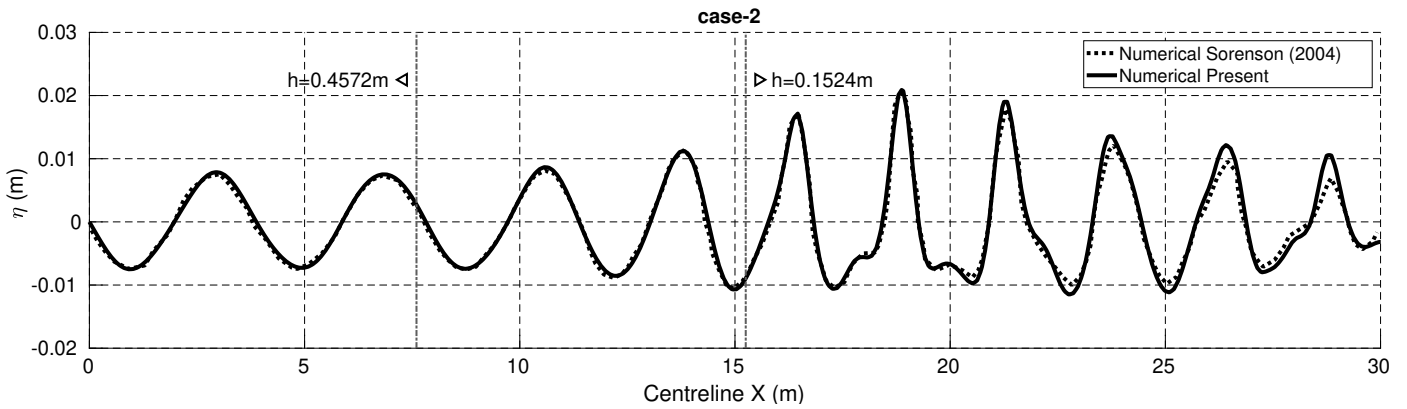


Figure 9: Numerical result for wave elevation measured along the centreline of the domain at  $t = 40\text{s}$  for case-2, compared against numerical results from [39]. The vertical lines at  $x = 7.60\text{m}$  and  $x = 15.25\text{m}$  mark the beginning and the end of the shoal along the domain centreline.

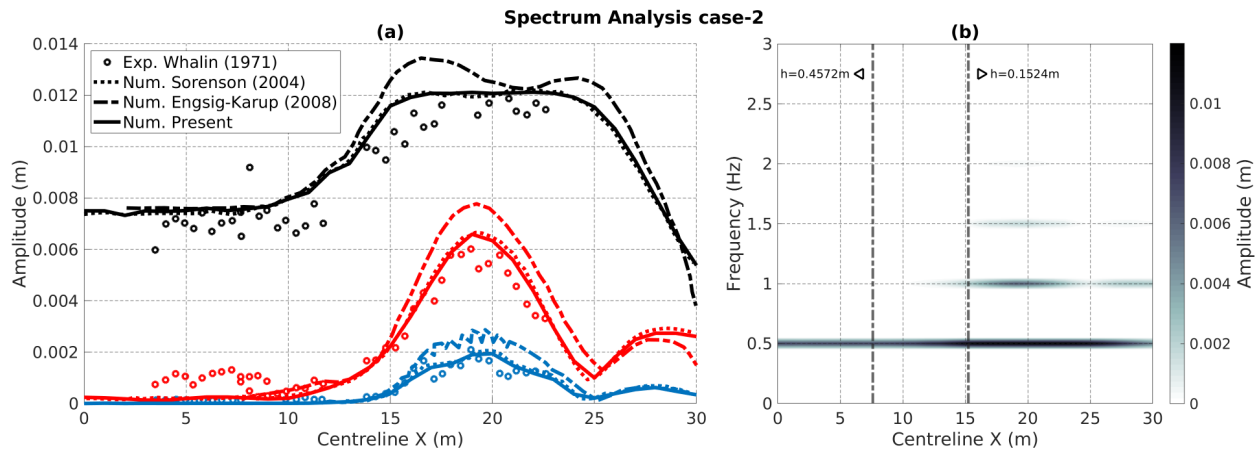


Figure 10: Spectral analysis for wave elevation along the centreline of the domain for case-2  $T = 2\text{s}$ . a) Comparison with experimental [46] and numerical [39, 44] results of amplitudes of the first (black), second (red) and third (blue) harmonics of wave elevation along the centreline. b) A spectrogram along the centreline showing the transfer of energy to higher harmonics behind the shoal. The vertical lines at  $x = 7.60\text{m}$  and  $x = 15.25\text{m}$  mark the beginning and the end of the shoal along the domain centreline.

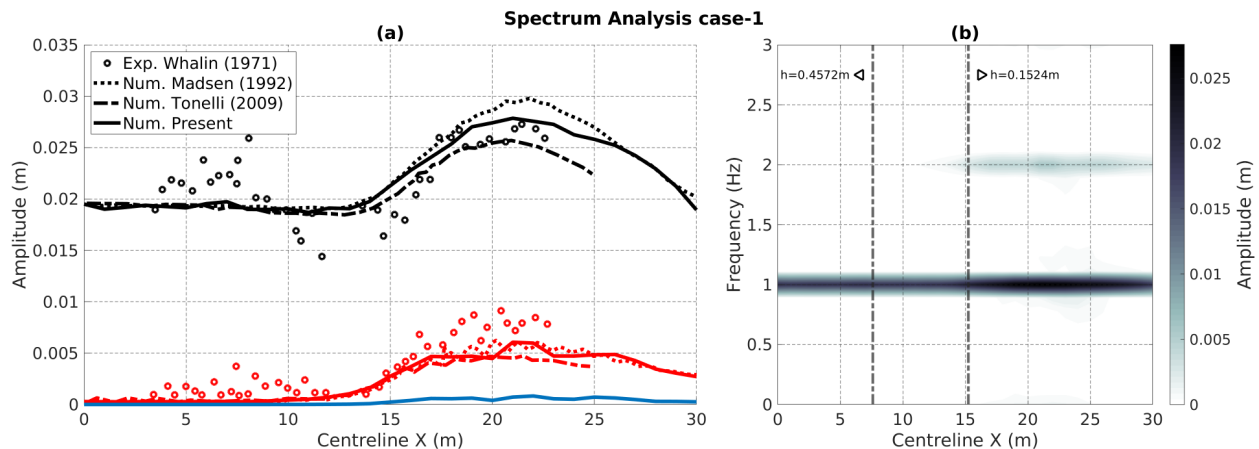


Figure 11: Spectral analysis for wave elevation along the centreline of the domain for case-1  $T = 1\text{s}$ . a) Comparison with experimental [46] and numerical [43, 56] results of amplitudes of the first (black), second (red) and third (blue) harmonics of wave elevation along the centreline. b) A spectrogram along the centreline showing the transfer of energy to higher harmonics behind the shoal. The vertical lines at  $x = 7.60\text{m}$  and  $x = 15.25\text{m}$  mark the beginning and the end of the shoal along the domain centreline.

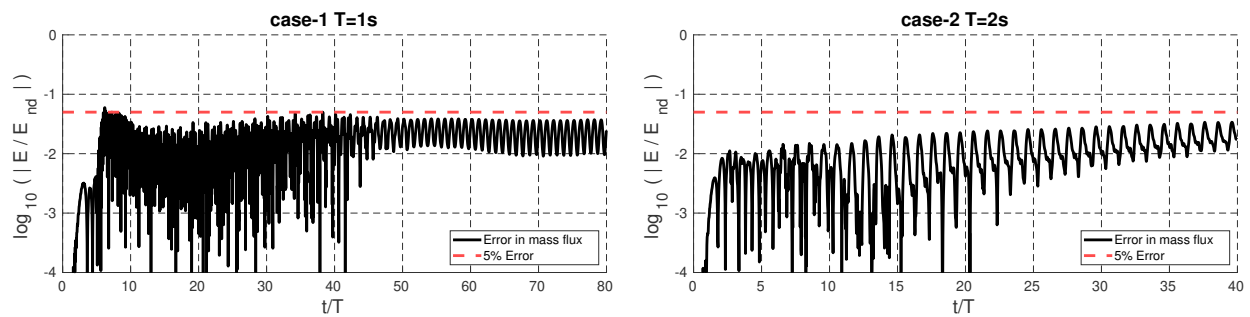


Figure 12: Plots reporting the error in conservation of mass by the presented numerical model during the entire duration of the simulation, for both case-1  $T = 1\text{s}$  and case-2  $T = 2\text{s}$ .

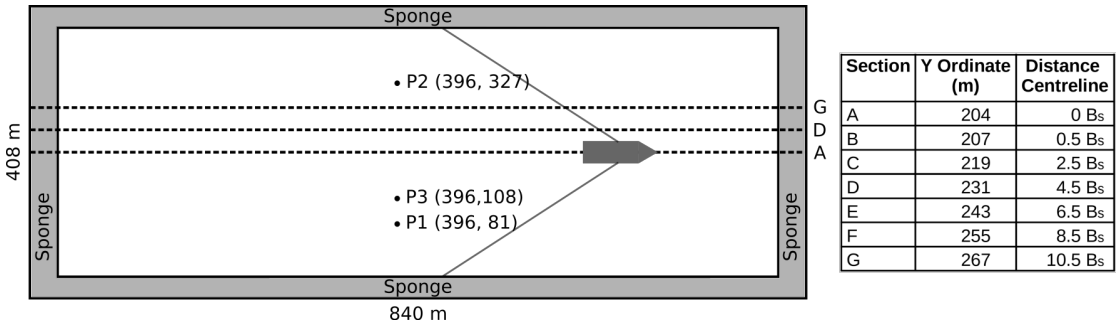


Figure 13: Schematic showing the simulation domain with the vessel moving along the centreline. The dashed lines indicate the sections along which wave elevation is measured. Additionally two point probes P1 and P2 are used to report temporal measurement.

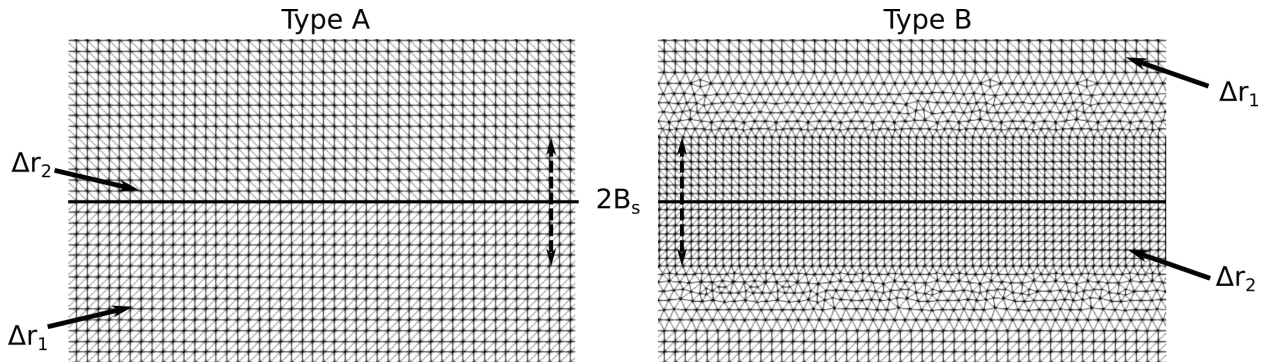


Figure 14: Samples of the two mesh types used for the simulation of vessel moving along the centreline. Type A is a constant resolution regular mesh. Type B has a finer resolution region of width  $2B_s$  around the vessel aimed at improving the capture of its pressure field.

the wave-length at cusps  $L_H = 16.90\text{m}$ . It is calculated using the analytical expressions from [58] in Appendix D. We conduct a brief mesh convergence study for this case. Two different kinds of meshes were tested as shown in Fig. (14). The characteristic mesh sizes are  $\Delta r_1$  in the outer domain and  $\Delta r_2$  in the close vicinity of the vessel. The Type A is a regular mesh with isosceles right angled triangles having  $\Delta x = \Delta y$  as the characteristic mesh size throughout the domain, with the orientation of the triangular elements mirrored about the centreline. The Type B mesh has a  $2B_s$  wide region of finer resolution  $\Delta r_2$  about the centreline for improved capture of the vessel's pressure field, and then it gradually transitions to a regular mesh of a coarser size  $\Delta r_1$  in the outer domain. The details of the tested setups are given in Table (2).

The coarsest setup is a Type B mesh M150B with  $\Delta r_1 = 1.5\text{m}$  corresponding to  $L_H/\Delta r_1 = 11.27$ , consistent with the recommendations in [2] for capturing the wave-system. Values of  $B_s/\Delta r_2 < 6$  were observed to be insufficient for capturing the pressure field. Therefore, this coarsest setup has  $\Delta r_2 = 1.0\text{m}$  corresponding to  $B_s/\Delta r_2 = 6$ . We present the mesh convergence for waves in the outer region away from the vessel through the P3 probe signal for the different setups as shown in Fig. (15). Table (2) also presents the error parameter  $P_d = \sqrt{\sum(\eta - \eta_{ref})^2 / \sum(\eta_{ref})^2}$  for P3 probe signal for each setup compared against the finest setup M050A. Further, the near-vessel convergence is observed using the derived quantity wave-making resistance  $F_x$ , calculated as described in section 3.2 for each setup and plotted in Fig. (16).

The coarsest setup M150B deviates from the finer setups in the wave-cusps region and in-fact it captures the transverse and divergent waves. The mesh for M100B is different from M100A in the vicinity of the vessel, where M100B has a finer resolution of  $\Delta r_2 = 0.75\text{m}$  instead of the  $\Delta r_2 = 1.0\text{m}$  in M100A, and has a smaller time-step of 0.10s instead of 0.125s. However their  $P_d$  are very similar, which indicates that the resolution around the vessel does not have a dominating effect on the outer waves once a sufficient resolution is achieved in vessel vicinity. We observe an overlap between the result from M075A and M050A in Fig. (15), and a low  $P_d = 0.1279$  for M075A, thus indicating convergence for outer flow. The near-vessel results observed through  $F_x$  indicate a fair agreement between M075A and M050A. However, the outer flow overlap is sufficient for our analysis. Further, we note that all setups had a Courant number in the range of 0.88 – 0.93 in these setups. The setup M075A was re-run with a smaller Courant number 0.47 in M075A-t2 to verify the time-step convergence. The  $P_d$  error for both of these setups are similar indicating a time-step convergence. Therefore the mesh requirement for this case is  $B_s/\Delta r_2 = 8$  near-vessel,  $L_H/\Delta r_1 = 22.54$  in the outer region. Finally, the Kelvin wave pattern for the aforementioned ship moving at  $Fr_d = 0.85$  obtained from the converged setup M075A is presented in Fig. (17).

The results from M075A are used for comparison against benchmarks. The first comparison is done for the Kelvin half-wedge angle  $\theta_K$  formed by the wave-cusps with the ship path. This comparison of numerically obtained  $\theta_K$  against the ana-

Table 2: Details of the simulation setups for pressure field in calm water.

Mesh name	Type	Resolution				Time step	Courant number	P3 Error $P_d$
		Outer $\Delta r_1$ (m)	$\frac{L_H}{\Delta r_1}$	Near vessel $\Delta r_2$ (m)	$\frac{B_s}{\Delta r_2}$			
M150B	B	1.50	11.27	1.00	6	0.1250	0.88	0.4585
M100A	A	1.00	16.90	1.00	6	0.1250	0.88	0.2374
M100B	B	1.00	16.90	0.75	8	0.1000	0.93	0.2397
M075A	A	0.75	22.54	0.75	8	0.1000	0.93	0.1246
M075A-t2	A	0.75	22.54	0.75	8	0.0500	0.47	0.1279
M050A	A	0.50	33.81	0.50	12	0.0625	0.88	Ref

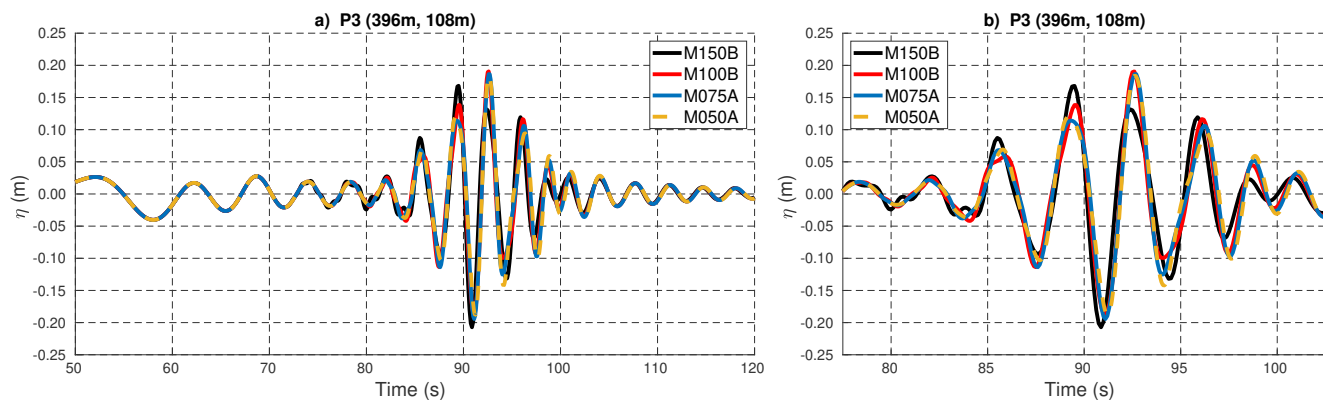
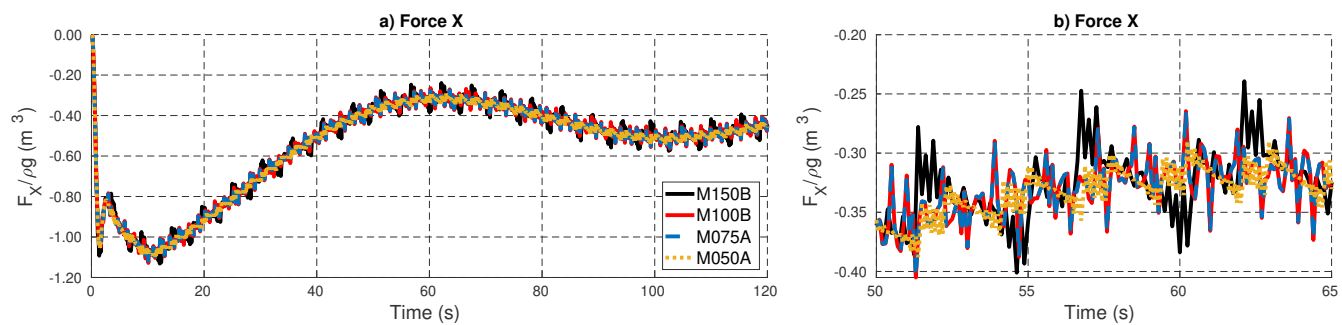


Figure 15: Plot of wave elevation at probe P3 for various simulation setups. It is used for establishing the mesh convergence. a) Zoom out view. b) Zoomed in view to highlight the wave-cusps.

Figure 16: Plots of estimated wave-making force  $F_x$  on the moving pressure field over time. a) Zoomed-out view b) Zoomed-in view.

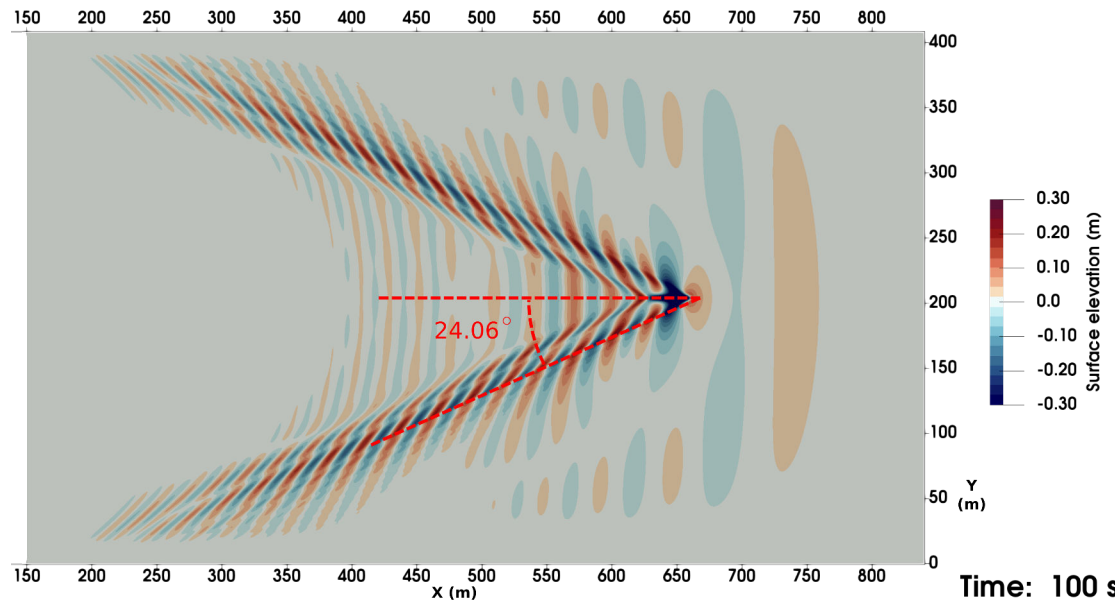


Figure 17: Contour plot of surface elevation obtained using M075A setup of our numerical model, with the highlighted half-wedge angle formed by the cusps.

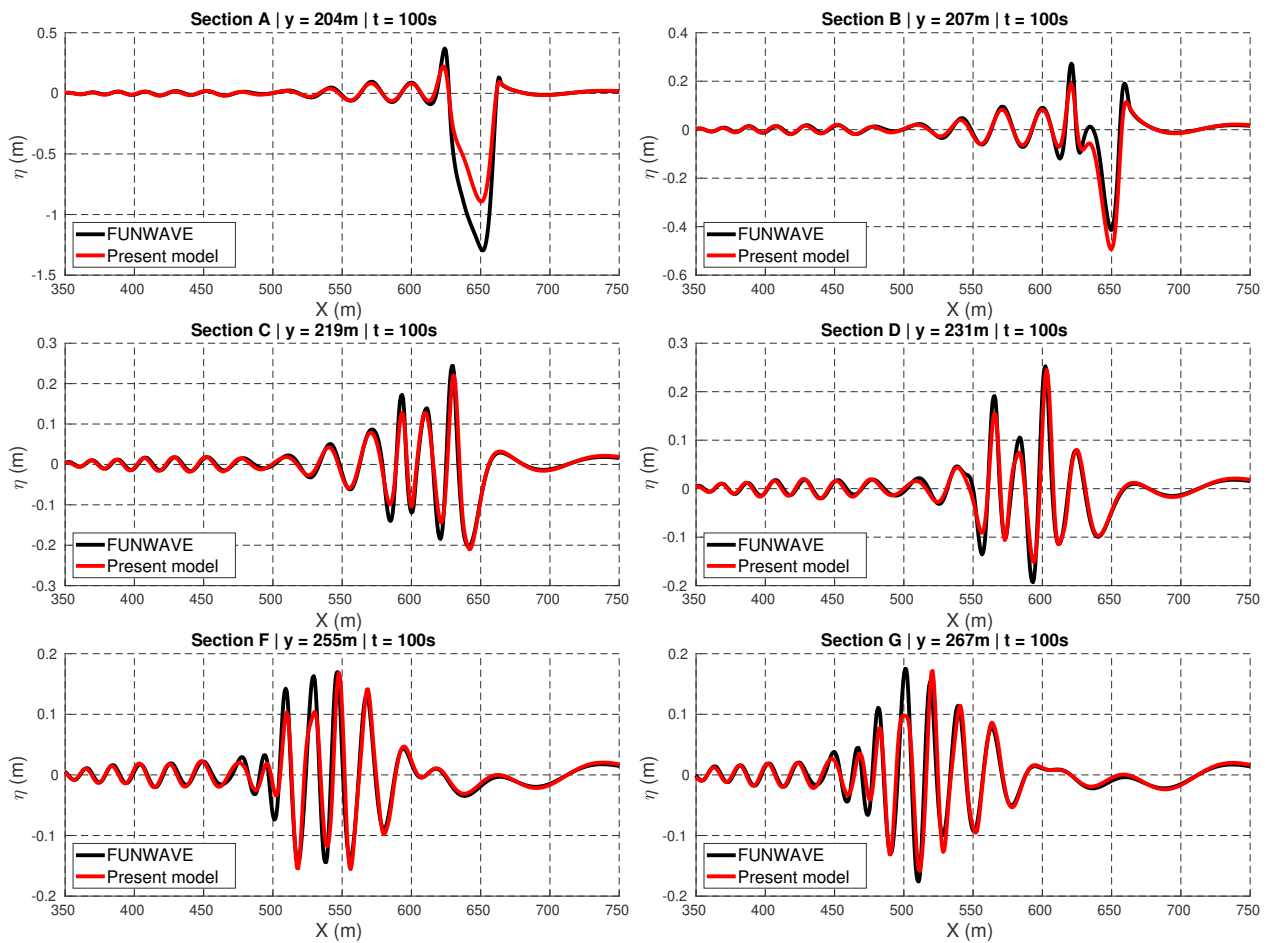


Figure 18: Comparison of results obtained from FUNWAVE-TVD and the present model FEBOUSS M075A for surface elevation at  $t = 100$  s along multiple sections of the domain

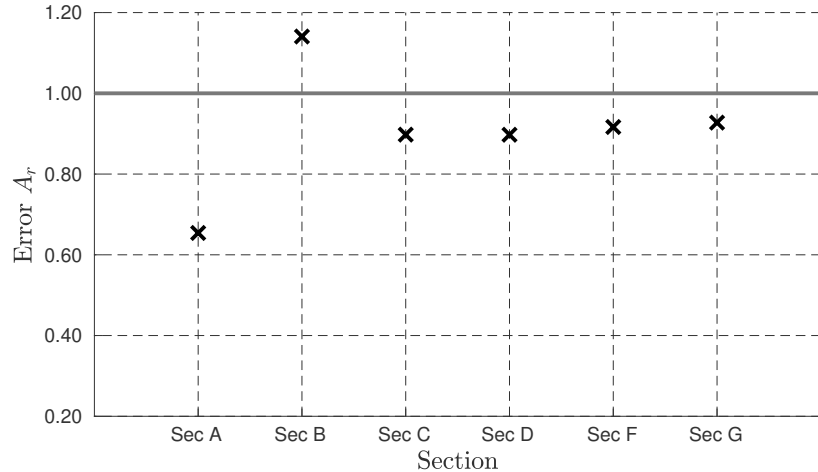


Figure 19: Plot of relative amplitude error parameters  $A_r$  quantifying the comparison of wave-elevation obtained from FEBOUSS M075A and FUNWAVE-TVD, measured along various sections.

lytical result is often presented as a validation case for wake generated by moving pressure field, as shown in [27, 28]. The analytical value is  $\theta_K = 24.76^\circ$  for  $Fr_d = 0.85$ , and was calculated using the expressions from [58] in Appendix D. We utilise the peaks of wave elevation obtained from FEBOUSS at section F and section G to calculate the numerically obtained  $\theta_K = 24.06^\circ$ . Hence, the difference against the analytical expression is a reasonable 2.83%. Fig. (17) highlights the numerically obtained  $\theta_K$  over the wave-elevation contour.

The results are further benchmarked against the same simulations done in FUNWAVE-TVD. The same domain with a regular quadrilateral mesh of size 0.75m with Courant number  $Cou = 0.2$  was used in FUNWAVE-TVD. The surface elevation at  $t = 100$ s is measured along various sections as shown in Fig. (13). The comparison between results from both the models is presented in Fig. (18). We have quantified the comparison of results using relative amplitude error parameter  $A_r = \sqrt{\sum(\eta_{FE})^2 / \sum(\eta_{FU})^2}$ , where  $\eta_{FE}$  and  $\eta_{FU}$  are wave-elevation along a section obtained from FEBOUSS and FUNWAVE-TVD respectively. A perfect agreement between the wave-elevations would result in  $A_r \rightarrow 1$ . Fig. (19) plots this for the wave-elevation measured along the various sections.

The major difference between the results from FEBOUSS and FUNWAVE-TVD is observed in the peak draft under the vessel as seen in the plots along section A between  $x = 630$ m and  $x = 680$ m. With the prescribed draft of the vessel being 1m, we observe from section A that FEBOUSS under-predicts the maximum draft. At the stern of the vessel a wave peak is generated as the flow converges after flowing around the vessel. This peak is higher in FUNWAVE-TVD than in FEBOUSS. Therefore section A shows a lower correlation between the models as seen with  $A_r = 0.64$ . Other than these differences in near-vessel region, the results from sections in outer region show some differences in the transition zone between divergent and transverse waves. However, as seen in Fig. (18) the results from both the models match fairly well, with similar frequency and amplitude of the transverse waves, and a good agreement of the divergent

waves in front of the cusps. Sections C-G have  $A_r$  values close to 1 indicating a fair agreement between the wave-elevations from FEBOUSS and FUNWAVE-TVD.

#### 4.4. Pressure field moving along a curved path

In addition to straight line paths, the moving pressure field implementation can be used for simulating ships moving along curved paths. For example, consider the case of ocean-going ships navigating the Hooghly river channel to access the major port of Kolkata in eastern India. The ships will have to negotiate multiple meanders along the river, similar to the highlighted Uluberia meander, as shown in Fig. (20a). In this particular example, the ships have to take up-to  $85^\circ$  turns at close to cruising speed to ensure the clearance of all the traffic within the high-tide period. A practical application of this would require the position and heading of the pressure field to be specified at certain time-instances, which may be irregularly spaced. Therefore, the path of the pressure field will have to be interpolated as per the simulation time-stepping requirements. In this section we demonstrate the significance of this path interpolation scheme.

We take a curved numerical domain as shown in Fig. (20b), overlapping the snapshot of the Uluberia meander obtained from Google Earth. The domain was made by picking points along the centreline of the river on Google Earth, connecting them through a spline and offsetting the spline by 250m on either side, creating a 500m wide curved domain. This waterway along the Hooghly river is regularly dredged to create a navigation path of 8m. Therefore, for this demonstration we have taken a fixed water depth of 8m throughout the domain. The inner and outer curves of the domain are walls and sponge layer of size 50m is placed on the remaining two boundaries for absorbing the waves. This curved channel is being used only to demonstrate the waves generated by ship moving along a curved path. A vessel of length 180m, breadth 30m and draft of 5m with shape defined by Eq. (8) is moved along the curved path at a constant speed of 10.5knots or  $5.4\text{m s}^{-1}$  correspond-

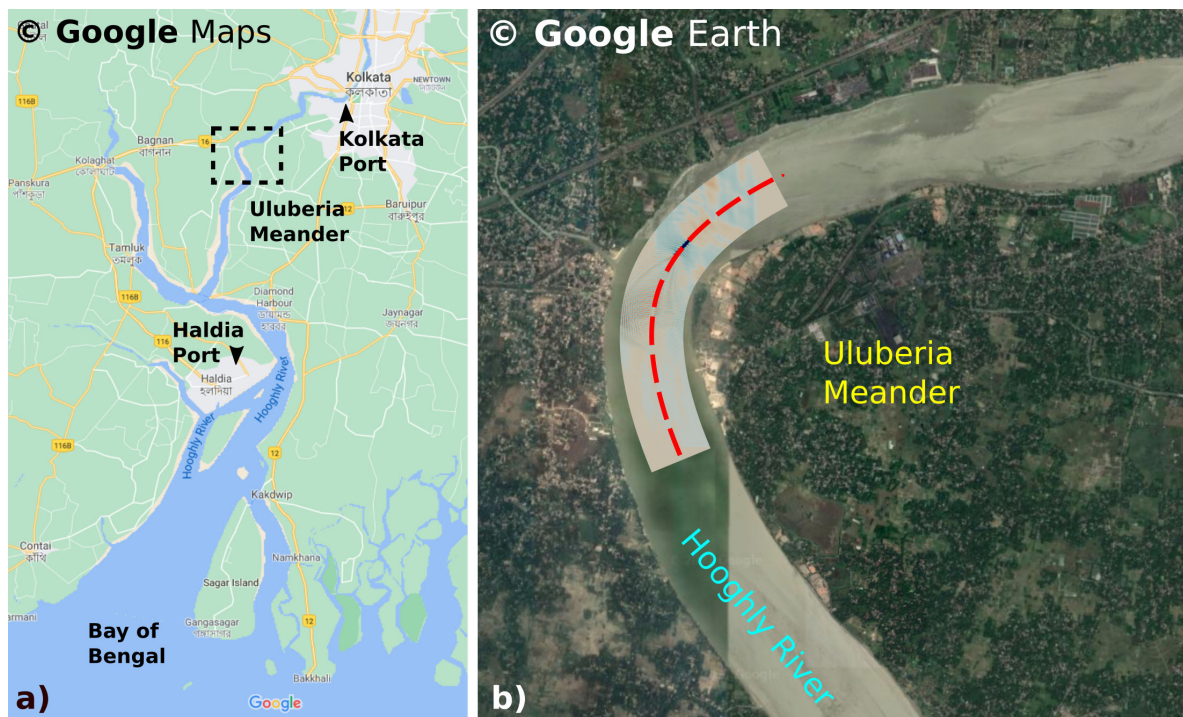


Figure 20: a) Snapshot from Google Maps showing the Hooghly river draining into the Bay of Bengal, with its meander near Uluberia highlighted. b) Snapshot of the meander near Uluberia  $22.4629^\circ \text{N}, 88.12^\circ \text{E}$  obtained from Google Earth with the superimposed. The dashed line is the curved path taken by the vessel.

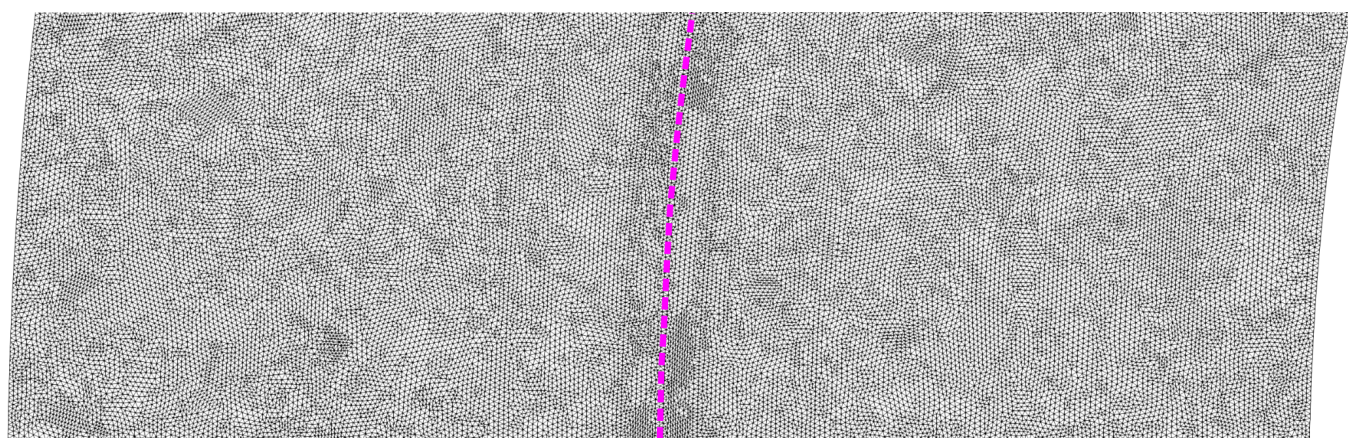


Figure 21: A section of the curved domain showcasing the unstructured mesh. The dashed line is the path of the pressure field.

ing to a Froude number of  $Fr_d = 0.6$ . These are representative of container vessel SSL Kutch (IMO 9157662) which is known to navigate this path to berth at Kolkata port. The unstructured mesh, as shown in Fig. (21), has a smaller resolution of 1.5m in a 60m band along the curved path of the ship. The rest of the domain has a mesh size of 1.75m, resulting in 926,721 triangular elements. The ship starts at the bottom of the domain and traverses a path of over 2.8km in 525s with the simulation running at a fixed time-step of 0.125s.

The path of the ship as shown in Fig. (20b) is specified using positions at irregular time-instances as given in Table 3. The interpolation of these positions as per the simulation time-stepping requirement is done using linear and natural cubic spline methods. Fig. (22a) shows the ship centre's interpolated position X between the user specified time instances (marked by the vertical grid-lines). In the  $C^0$  continuous linear interpolation, the derivatives  $\partial X/\partial t$ ,  $\partial Y/\partial t$  and  $\partial \theta/\partial t$  will be discontinuous across the user specified time-instances. The effect of this can be seen in the force Y plot in Fig. (22b), where numerical shocks are observed after each user specified time-instant. A more visual manifestation is seen Fig. (23), where the contour plot of surface elevation is presented at  $t = 300$ s for both interpolation methods. In case of linear interpolation, ripples are created due to the sudden change in the rate of position and heading. In reality, the ships cannot make a sudden turn like this and will instead make smooth turns. Therefore the  $C^2$  continuous natural cubic spline method ensure a more realistic result through continuous derivatives up-to second order. The resultant smooth path for the ship avoids any unnatural shocks or ripples as seen in the force plot and surface elevation contour. Therefore, in order to simulate ship motion along arbitrary paths, it is crucial to avoid linear-interpolation of the path.

#### 4.5. Waves generated by fast moving ferry in Tallinn Bay

This section presents real world application of FEBOUSS for simulating waves generated by moving vessels, along with validation against field measurements. We utilise the field measurements from Tallinn Bay, which is a  $10\text{km} \times 20\text{km}$  region on the north-eastern end of Baltic sea along the northern coastline of Estonia, as shown in Fig. (24a). It is flanked by Estonia's capital city of Tallinn on the south, island of Naissaar on the north-west, Viimsi Peninsula on the east and Aegna island on the north-east as shown in Fig. (24b). Due to these landmasses, the bay is fairly protected from winds with the mean significant wave-height  $H_s$  of wind-generated waves below 0.5m and occasional rough seas with  $H_s$  in 3m – 4m range [59]. Fig. (24b) shows the navigation path taken by vessels to access the major passenger port of Tallinn from Gulf of Finland. It is a heavy traffic route used by large passenger vessels, including high-speed ferries servicing the Tallinn-Helsinki ferry link. In the summer of 2008, the ferries from this link alone accounted for 20 crossings per day in each direction. Typical wind waves in this region have a period below 3s, however the ship-generated waves can often be of 10 – 12s. Due to the mild wind conditions in this region, the waves generated by these vessels contributed to 5 – 8% of total wave energy and 18 – 35% of wave power as reported in [59]. Therefore, extensive field measurements

were done to study the impact of ship-generated waves on the surrounding coastline. We use the measurements from the summer of 2008 campaign which is detailed in [22].

The navigation path shown in Fig. (24b) is along a trench in the local topography. This trench is seen in the depth contours for the bay region in Fig .(25a). The north-bound vessels move close to the east coastline, with Aegna island being closest to the path at 2km. By the time the vessels approach the island, they have accelerated to their design speed [33]. Therefore the southern and western coastlines of Aegna island are heavily exposed to ship-wakes. The campaign in June-July of 2008 as reported in [22] took field measurements for wave-elevation at a mixed sand-gravel beach on the south-west end of Aegna island as shown in Fig .(25a) with annotation WGA. The measurements were taken using an ultrasonic echo-sounder mounted on a tripod about 100m from the coast at a sampling frequency of 5Hz. WGA is located at ( $56^\circ 34.26' \text{ N}, 24^\circ 45.36' \text{ E}$ ) with local water depth of 2.8m during the observation period. Using this setup, measurements of ship-wakes due to various large vessels navigating this path were reported in [22].

We use the data measured for mono-hull high speed ferry *SuperSeaCat* on 29-June-2008. This data-set has been used in a number of numerical [32, 33] and analysis publications [60, 61]. The vessel has length of  $L_s = 100.3\text{m}$ , beam  $B_s = 17.1\text{m}$  and draft  $D_s = 2.6\text{m}$  with design speed of 35knuts  $\approx 18\text{m s}^{-1}$ . The position and speed of this ferry were recorded using GPS every second. The actual path of the ship is plotted in Fig .(25a). Numerical simulation for this case was done using a highly-nonlinear Boussinesq equation model COULWAVE [8, 9] and the comparison against field measurements was reported in [33]. We will follow a similar approach for validating FEBOUSS results against the field measurements. The COULWAVE simulation in [33] were done using a  $7.5\text{m} \times 7.5\text{m}$  rectangular grid. They have reported attempting a finer mesh resolution of 5m. However this resulted in numerical instabilities in COULWAVE due to grid scale noise [33]. They have used the pressure field with dimensions  $L_s = 100\text{m}$ ,  $B_s = 40\text{m}$  and  $D_s = 1\text{m}$ , with the shape defined by Eq. (6) and coefficients  $\alpha_1 = \alpha_2 = \beta_1 = 0.75$ . We denoted this shape as SSB40. Please note the difference in the beam and draft of the actual vessel and the pressure field. We believe the wider beam was used due to the coarse mesh size of 7.5m and therefore a lower draft was used to maintain the displacement of the vessel. The change in pressure field dimensions is expected to have limited influence over the long waves. We simulate this case in FEBOUSS using pressure field with dimensions  $L_s = 100\text{m}$ ,  $B_s = 18\text{m}$  and  $D_s = 2.6\text{m}$ , with the shape given by Eq. (6) with coefficients  $\alpha_1 = \alpha_2 = 0.75, \beta_1 = 0.50$ . These parameters denoted as SSB18 are closer to the real ship dimensions and have the same displacement as SSB40.

We have taken a numerical domain of size  $4500\text{m} \times 7800\text{m}$  by considering the ship path and the probe location. The position of this domain within the bay is show in Fig .(25a) The bathymetry data was provided at a resolution of  $0.5' = 463\text{m}$  longitude and  $0.25' = 470\text{m}$  latitude [33]. This is mapped on to the numerical domain as shown in Fig .(25b). Due to inaccuracies in the given bathymetry data, the local depth at

Table 3: Table listing the ship centre's position ( $x_s, y_s$ ) and heading  $\theta_s$  specified as user inputs to the program at certain time-instances to make the ship move along the curved path.

$t(s)$	0	24.67	47.90	91.10	134.31	177.49	220.66	...	593.77
$x_s(m)$	272.11	222.39	179.36	111.44	62.83	39.92	51.87	...	1468.80
$y_s(m)$	1471.9	1595.5	1713.3	1936.5	2164.6	2396.7	2629.5	...	3950.4
$\theta(^{\circ})$	111.91	110.07	106.92	102.03	95.64	87.06	75.54	...	28.68

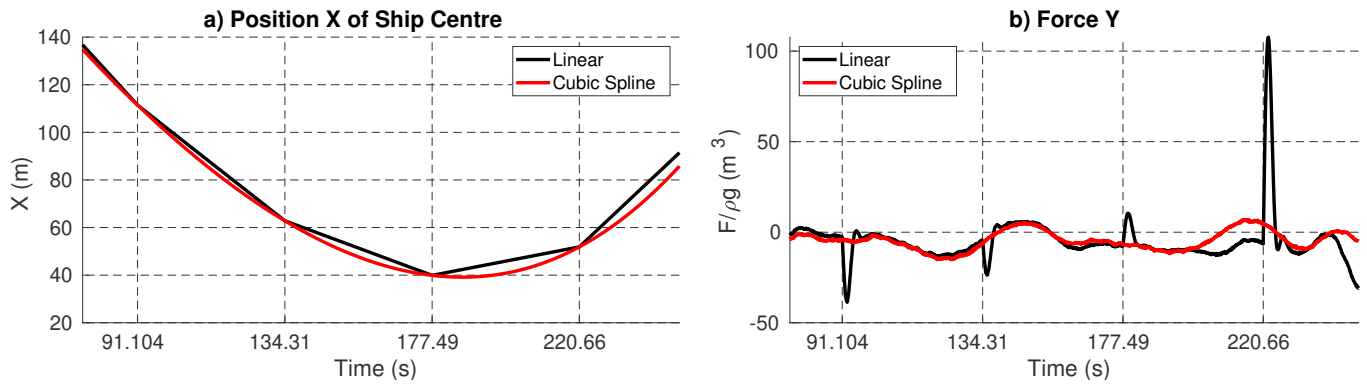


Figure 22: a) Plot of ship centre's position interpolated between user given points (marked by the vertical grid-lines) using linear and cubic spline methods. b) The discontinuous gradient in linear method results in shocks in the simulation which is seen in the force Y plots.

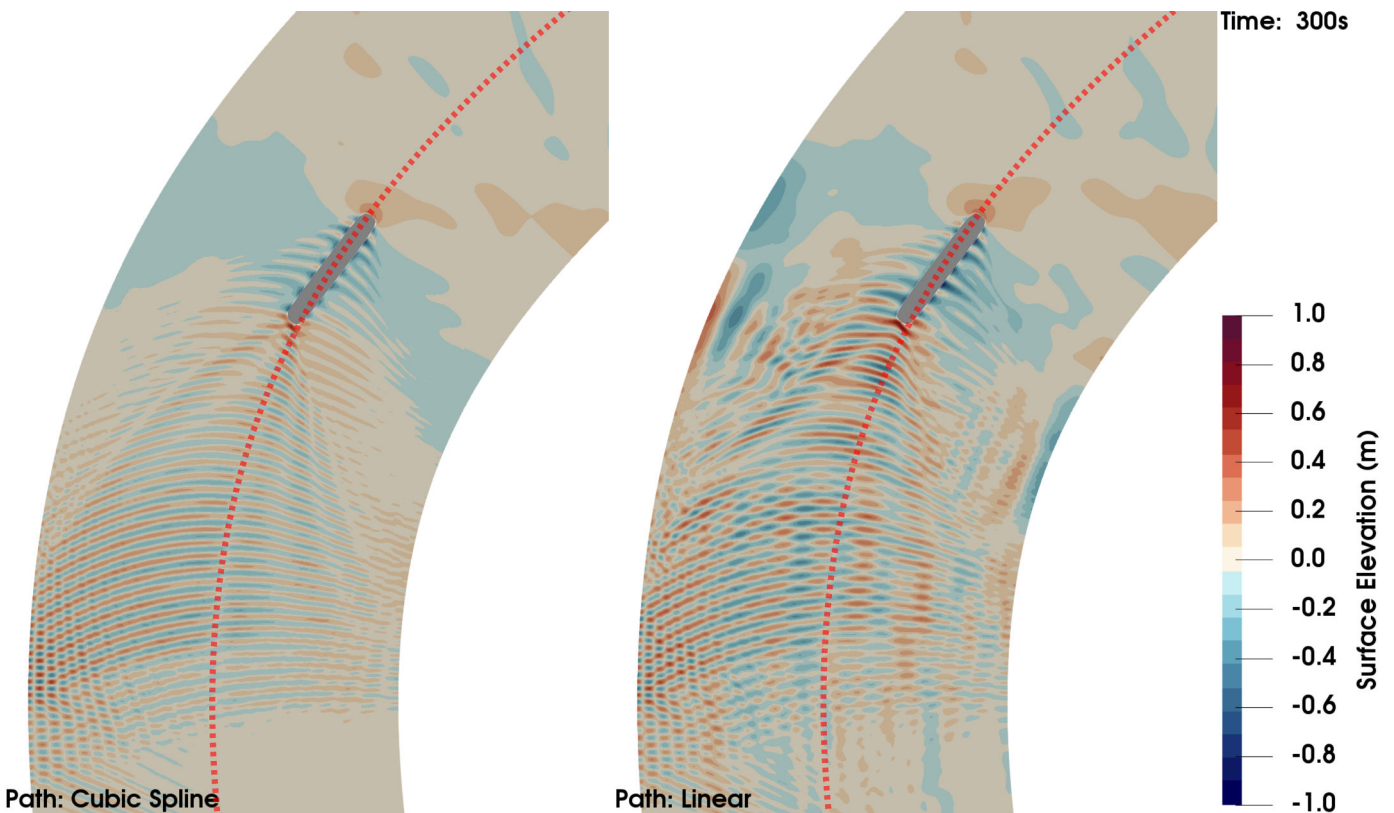


Figure 23: The surface elevation contours showing the significance of cubic spline interpolation of ship's path against the linear interpolation of ship's path. The dashed line is the path taken by the vessel.

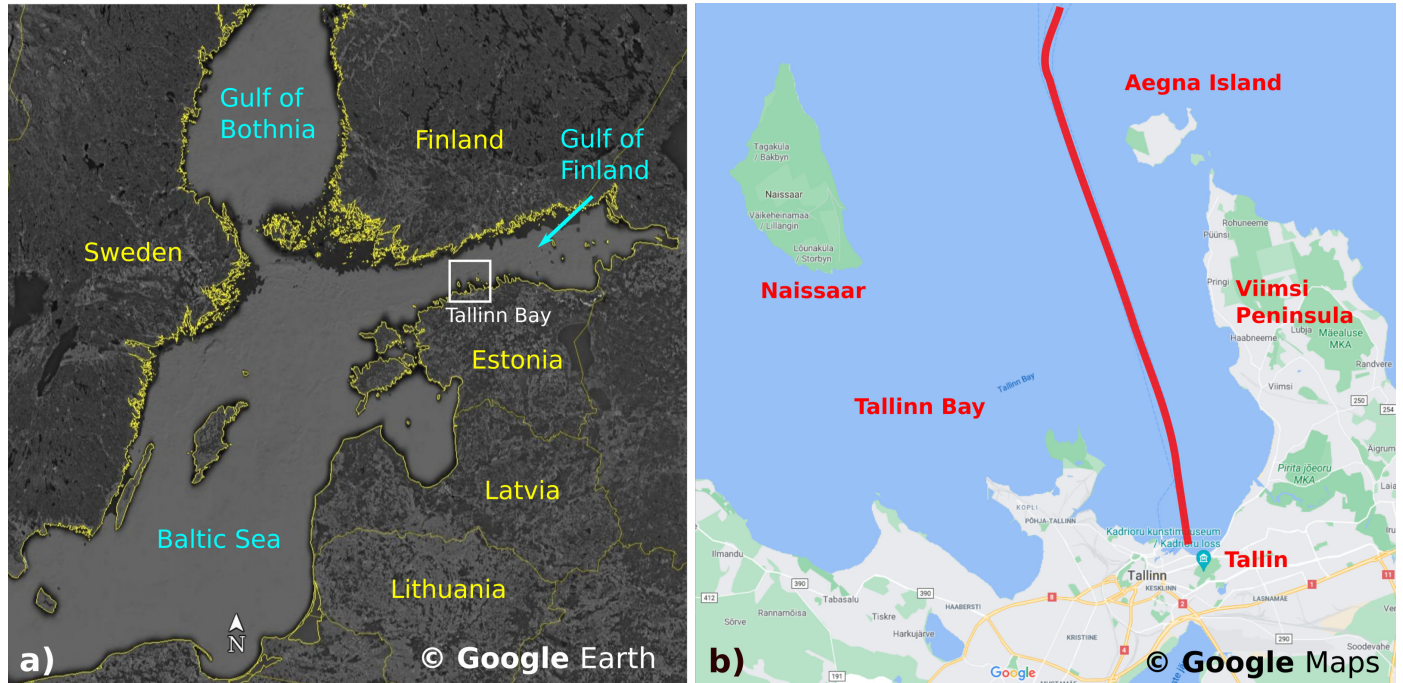


Figure 24: a) Map highlighting the location of Tallinn Bay along the northern coastline of Estonia. b) Map of Tallinn Bay region obtained from Google Maps ( $59.4964^{\circ}$  N,  $24.6562^{\circ}$  E) showing the important landmasses surrounding the bay. The solid line indicates the route taken by vessels to access Tallinn port from Gulf of Finland.

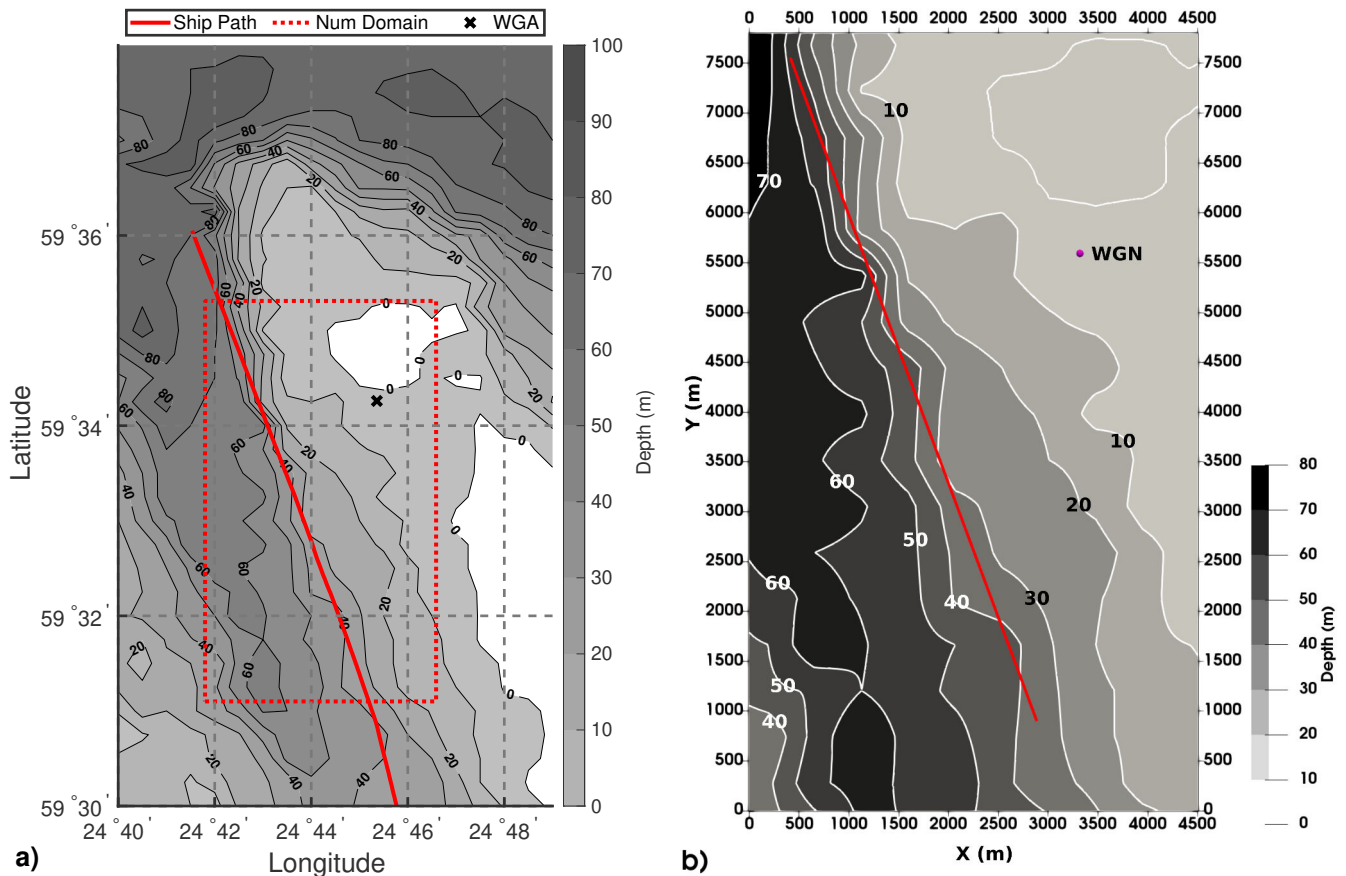


Figure 25: a) Contour plot for water depth in Tallinn Bay. The dashed line shows the location and size of the numerical domain. The solid line is the measured path taken by the ferry *SuperSeaCat*. The cross shows the location of wave gauge WGA used for measuring the wave impacting Aegna island. b) Plot showing the numerical domain with depth contours. The simulated ship path is shown by the solid line. The numerical measurement of surface elevation are reported at WGN.

WGA in the numerical domain is 1.2m instead of the measured 2.8m. Therefore, we use a nearby location WGN at ( $56^{\circ} 34.12' N, 24^{\circ} 45.33' E$ ) for reporting the numerical results, similar to the COULWAVE simulations for this case in [33]. We simulate a portion of the ship's path as shown in Fig. (25b). The starting position for the pressure field is about 4.7km from WGN, to allow for the development of the wake patterns. The GPS track indicates the ship moving at a speed of  $15.96 m s^{-1} \approx 31$  knots along this path. The waves reaching WGN are thus generated while the ship moves in depth of range 29m – 53m with the depth Froude number in range 0.69 – 0.94. The pressure field is started without acceleration and follows the GPS tracked path of the ship.

We use an unstructured FEM mesh with irregular triangles. It is generated using ANSYS Meshing software. The domain is divided into various sections as shown in Fig. (26). Following the analysis from section 4.3, a band of triangles with side 5m along the ship length direction and 2m along the ship beam direction was generated to accommodate the narrow beam of  $B_s = 18$ m in SSB18 as shown in Fig. (26a). The majority of the remaining domain consists of irregular triangles and isosceles right-angled triangles with size 5m as shown in Figs. (26b) and (26c). Sponge layers of width 500m are placed along the east, west and south boundaries, and a width of 1000m along the north boundary. This is done to ensure absorption of the long waves. The mesh size in these sponge layers transitions from 5m to 10m, as shown in Fig. (26d). Overall the domain consists of 2.43 million triangular elements. As mentioned in section 2, the present model does not include wave-breaking. Bottom friction is implemented using quadratic law as per Eq. (3), using Manning coefficient = 0.033. The simulation time-step is constant at  $\Delta t = 0.1$ s, corresponding to Courant number  $Cou = 0.97$  in the narrow band along the ship's path due to the triangles with side 2m, and  $Cou < 0.5$  throughout the remaining domain.

The surface elevation contours obtained from FEBOUSS for SSB18 are shown in Fig. (27a). As the ship follows the path in the trench, the waves undergo refraction and shoaling over the steep slopes of the trench. The waves thus turn towards Aegna island, heading directly for its south-western coastline. This is line with the observations in [59] and simulations in [32, 33], where the south-western coast of Aegna is termed as a "hot-spot" for the impact of ship generated waves.

The numerical results at WGN are compared against field measurements in Fig. (28). The field measured results are filtered with low-pass filter at a cut off frequency of  $0.29\text{Hz} = 3.5\text{s}$  to minimise the wind generated waves. FEBOUSS time-series for SSB18 in Fig. (28a) match fairly well with the field measurements, especially in the wave amplitude. The difference in phase beyond  $t = 510$ s is likely due to the limitations of the wave damping. The amplitude spectrum in Fig. (28b) shows the primary peak period of 10.22s from FEBOUSS SSB18, which is within 4.3% of the field measured peak of 10.68s. However, the numerical results for higher frequencies are muted in the time-series and the spectrum. Considering the inherent approximation of pressure field moving in 2DH model, with a relatively coarse resolution for the bathymetry, the obtained results are

fairly functional for simulating waves generated by ship moving in 3D space.

We have also carried out the FEBOUSS simulation using ship shape SSB40, similar to the COULWAVE simulations in [33]. By comparing the contour plots in Fig. (27a) for SSB18 and Fig. (27b) for SSB40, we observe that due to the wider beam and lower draft of SSB40, it does not generate certain high frequency waves. For example, we can observe this in the wave elevation along a line section at  $y = 5350$ m as shown in Fig. (29a). The time-series in Fig. (28a) in the shallower depth of WGN shows a marginal difference between the results from the two shapes. On a closer look through the spectrum in Fig. (28b), we observe lower amplitudes of high frequencies for SSB40 when compared with SSB18. However, the limited difference in the results from SSB18 and SSB40 indicates that waves away from the vessel are largely dependent on the length and displacement of the pressure field. When compared with the COULWAVE results, which were digitised from [33], the FEBOUSS result for both shapes SSB18 and SSB40 show an improved agreement against the field measurements.

The variation of wave-making resistance against the surge direction, estimated using Eq. (13), while the ship moves in changing water depth is shown in Fig. (29b). We observe the expected trend of direct correlation between the wave-making resistance and depth Froude number. The values for SSB40 are about 20% lower than SSB18, thus highlighting the difference in near-vessel flow due to the change in the shape of the pressure field. The vessel *SuperSeaCat* has a total installed propulsive capacity of 27.5MW. The wave-making resistance obtained from SSB18 as shown in Fig. (29b) is in the range of 550 – 900kN, which corresponds to 8.8 – 14.4MW power for the vessel moving at 31knots. However, a direct comparison of the estimated and real wave-making resistance could not be established in this exercise.

This section thus provided a validation for FEBOUSS against field measurements using a problem involving moving vessel and variable bathymetry. The approach followed here can be used for identifying regions sensitive to ship-wakes in high traffic areas. Further, it can be used to alter the navigation paths for minimising the impact on surrounding coastline.

## 5. Conclusion

The paper has presented development of an unstructured finite element model (FEBOUSS) based on Madsen and Sørensen's form of Boussinesq equations for simulation of free surface flows. The model employed standard Galerkin method with mixed linear and quadratic shape functions; analytical integration of elemental integrals; and a stable time-marching through Runge-Kutta 4<sup>th</sup> order method. It was verified through comparisons against experimental and numerical results for wave transformation over the complex Whalin shoal. We also demonstrated the mesh and time-step convergence of the model and reported the conservation of mass.

Simulation of ship-generated waves in finite water depth was implemented in FEBOUSS by using a moving pressure field.

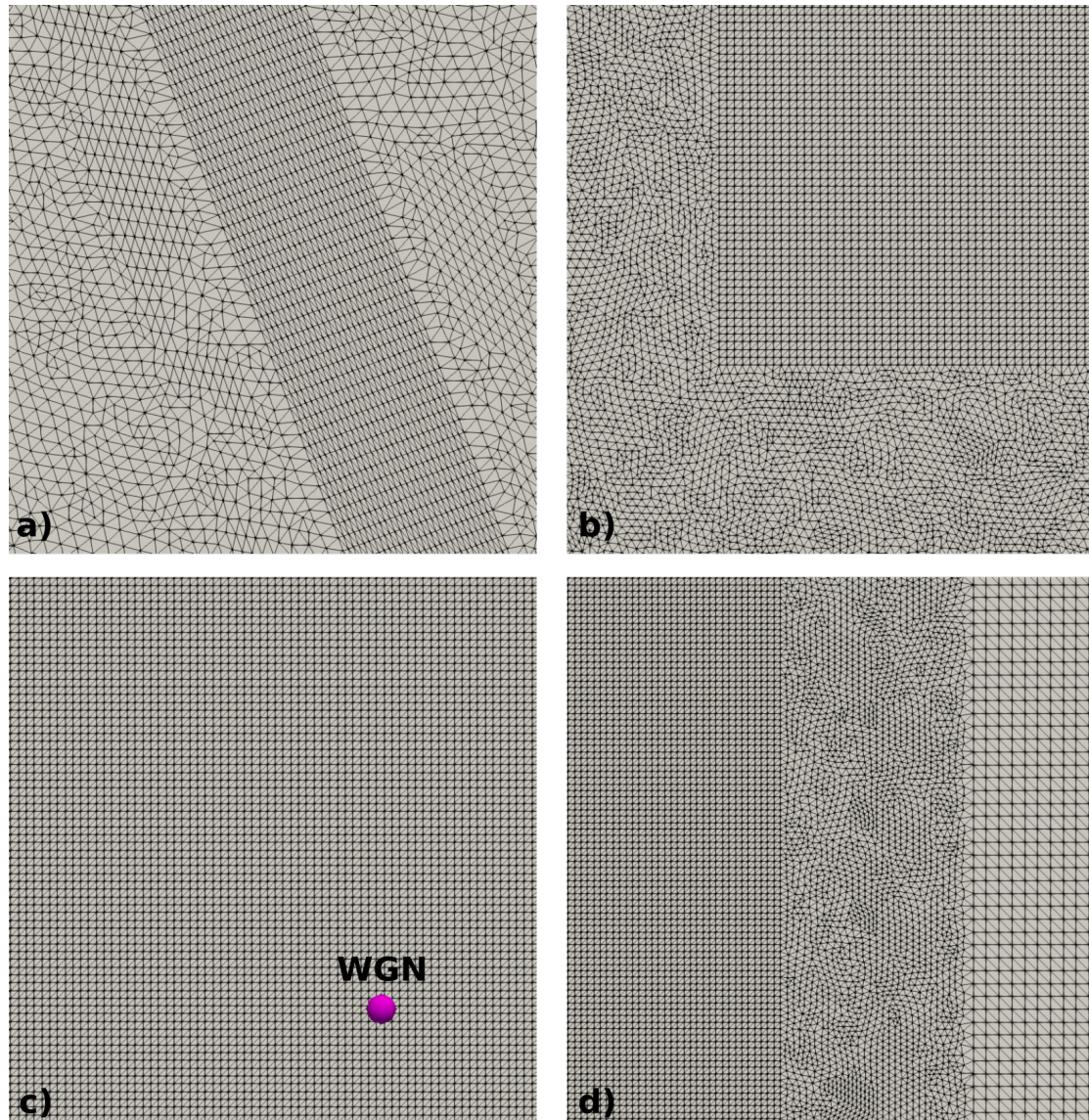


Figure 26: Various sections of the FEM mesh. a) A band along the ship's path with small resolution to capture the beam of the pressure field. b) Mesh transitioning from irregular triangles to regular triangles. c) Regular mesh around the measurement location WGN. d) Mesh transitioning to coarser resolution in the sponge layer.

Shape of the vessel was prescribed through analytical expressions. The wave-making force was estimated through gradient of surface-elevation, which was calculated using a mesh-free approach. This estimated force may not be accurate but can be useful in drawing practical conclusions. These methods can simulate multiple ships moving along arbitrary paths. A simulation for ship moving along a straight path in finite depth was presented. We conducted a convergence analysis and prescribed the mesh and time-step requirements for capturing the vessel profile and the dominant waves. The results for surface elevation were compared against similar simulations done in FUNWAVE-TVD. We also simulated a ship moving along the curved path of a river channel, and highlighted the requirement of smooth interpolation of the ship's path at simulation time-step.

The paper finally presented a real world application by sim-

ulating waves generated by a fast-ferry in Tallinn bay region in Estonia using FEBOUSS. The unstructured grid enabled local refinement of the mesh along the ship's path, thus allowing capture of the relatively narrow beam of the vessel. The results showcased the concentration of ship-generated waves towards a particular landmass due to the local bathymetry. Further, the results were validated against field measurements for wave elevation. We also investigated the impact of modifying the ship's beam and draft while keeping the length and displacement constant. With the modified dimensions, no significant difference was observed in the long waves away from the vessel. However, the near vessel flow was missing high frequency waves for the wider shape. This example demonstrated the application of FEBOUSS and similar models for identifying regions which are sensitive to ship-generated waves in high-traffic regions.

The key highlight of this manuscript is the presentation and

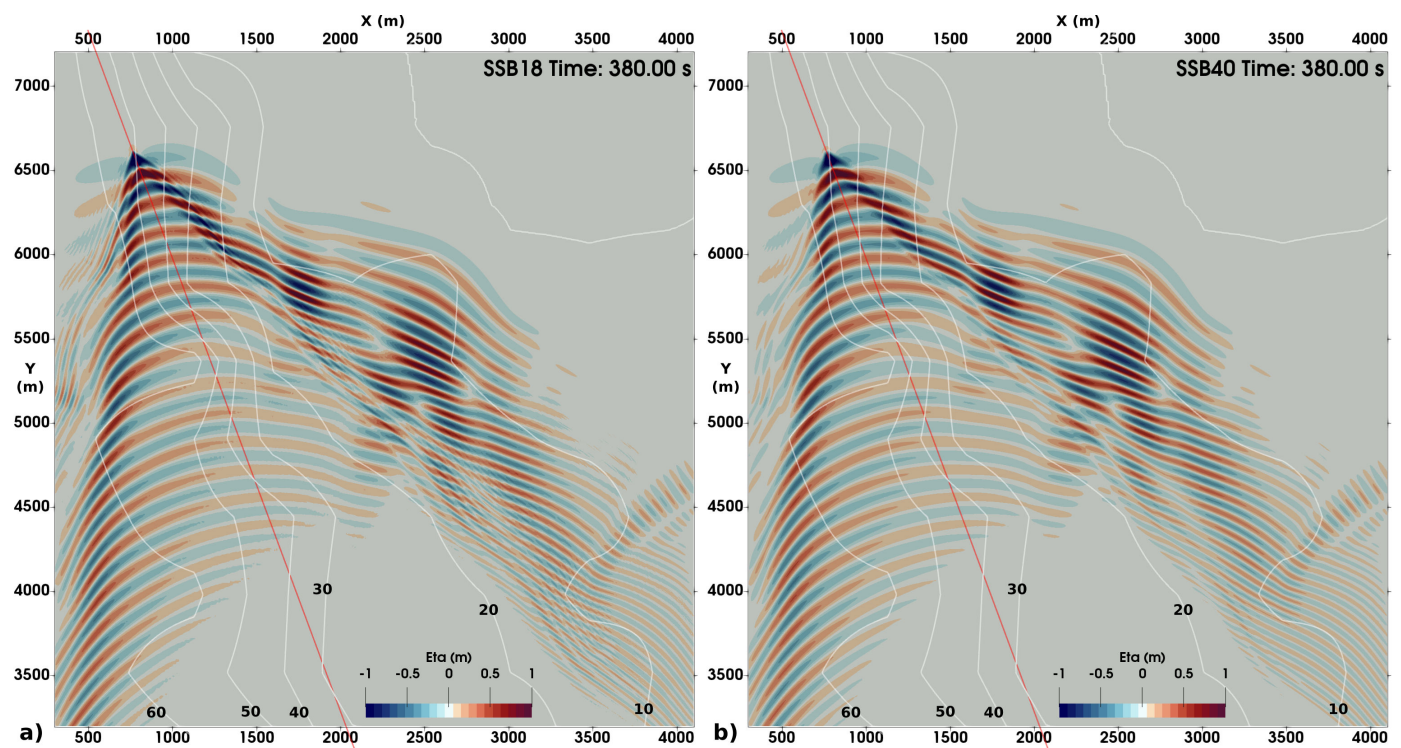


Figure 27: Plot showing filled contour plots for surface elevation  $\eta$  at  $t = 380$ s in a portion of the numerical domain. The white lines are water depth contours with the depth mentioned in meters. The red solid line is the ship's path. a) Ship shape SSB18 b) Ship shape SSB40

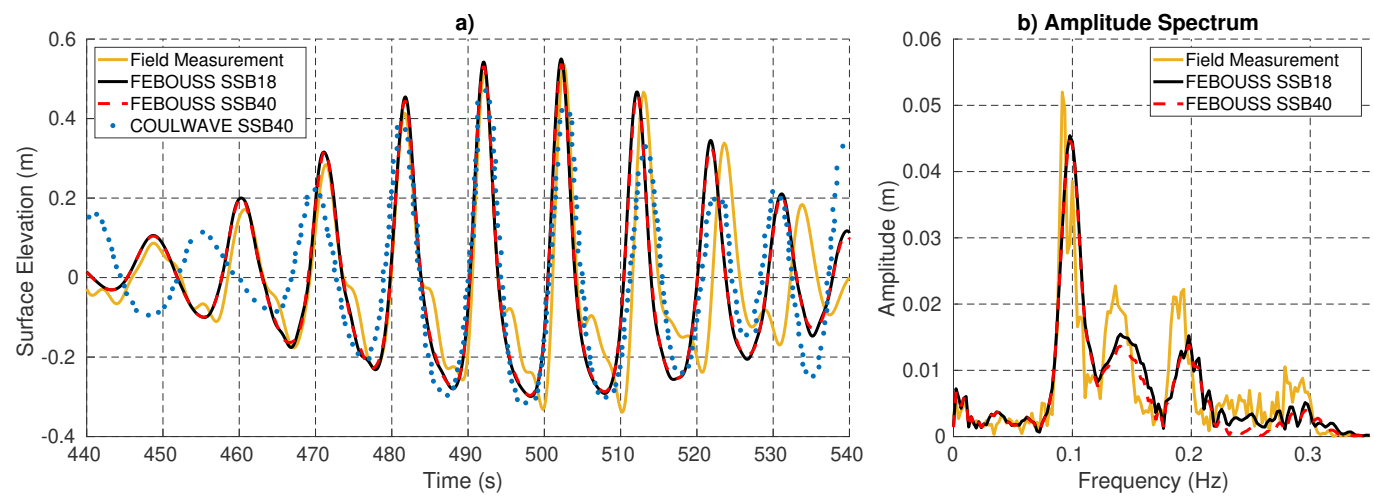


Figure 28: a) Comparison of surface elevation obtained from field measurements, numerical results by FEBOUSS from the present work and numerical results by COULWAVE digitised from [33]. b) Comparison of amplitude spectrum obtained from the field measurements and FEBOUSS simulations.

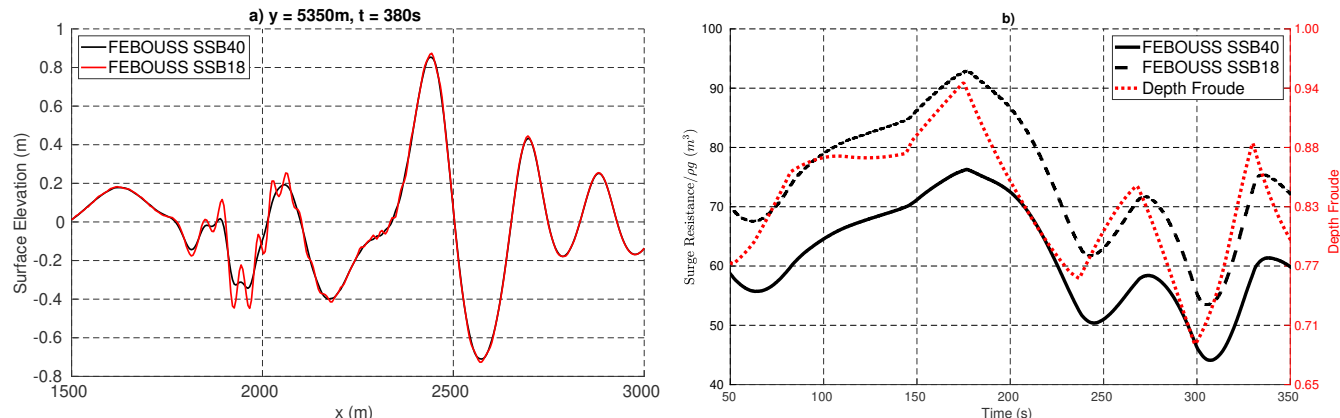


Figure 29: a) Wave elevation obtained from FEBOUSS along a portion of  $y = 5350\text{m}$  at  $t = 380\text{s}$  comparing the results from pressure fields with shape SSB18 and SSB40. b) Instantaneous wave-making resistance against the surge direction estimated using Eq. (13) plotted over time along with the depth Froude number for the pressure field.

investigation of a stable finite-element model capable of simulating wave-transformation over uneven bathymetry. The implementation over unstructured triangular grid allows for local mesh refinement which is crucial for capturing the multi-scale physics over large domains. Further, the implementation of pressure field moving along an arbitrary path enables efficient reproduction of the ship-generated waves for practical applications, such as mooring loads and sediment transport in sheltered harbour.

This work has set the basis for applying FEBOUSS for simulating a variety of scenarios. Building on this, further developments by inclusion of sediment transport, wave-breaking, tidal and current effects can improve the practical functionality for field application of this model in estimating shoreline evolution. Additional research will be required to specifically identify the correlation between the physical dimension of a vessel and the dimensions of the corresponding pressure field in the context of simulating ship-generated waves. A correlation could also be established between the real wave-making force and the approximation presented in this manuscript. In terms of applications, the future work could also study the interaction between wakes of multiple vessels in a harbour. Further, this 2DH model can be coupled with 3D viscous flow model to enable accurate and efficient simulation of large-domain problems while incorporating different physics.

## 6. Acknowledgement

The first author acknowledges the support of Prime Minister's Research Fellowship (PMRF), India in funding this research work. We would like to acknowledge NTCPWC, Ministry of Shipping, India for funding the project "Assessment tool for assessing the impact of Ship/Boat Wake Waves on the banks and protection measures for Inland National Waterways". P. L.-F. Liu would like to acknowledge the supports from the VAJRA Faculty Scheme of India, National University of Singapore, Cornell University, and the National Research Foundation through a grant to the National University of Singapore (Award number:NRF2018NRF-NSFC003ES-002. This

research was also supported in part by Yushan Program, Ministry of Education in Taiwan. The authors thank Dr. Ira Didenkulova from University of Oslo, Norway for providing the field measurement data for section 4.5. The authors thank the anonymous reviewers and editor for their constructive feedback on the manuscript.

## Declaration of interests

The authors report no conflict of interest.

## Author ORCIDs

**S. Agarwal:** <https://orcid.org/0000-0003-1922-4242>

**V. Sriram:** <https://orcid.org/0000-0003-3586-9577>

**P. L.-F. Liu:** <https://orcid.org/0000-0002-2170-5507>

**K. Murali:** <https://orcid.org/0000-0002-4251-841X>

## Author contributions

**S. Agarwal:** Conceptualisation, Software, Validation, Formal analysis, Methodology, Writing – original draft, Visualisation.

**V. Sriram:** Conceptualisation, Methodology, Writing – review and editing, Funding acquisition, Supervision.

**P. L.-F. Liu:** Conceptualisation, Writing — review and editing. **K. Murali:** Writing – review and editing, Funding acquisition, Supervision.

## References

- [1] D. H. Peregrine, Long waves on a beach, *Journal of Fluid Mechanics* 27 (4) (1967) 815–827. [doi:10.1017/S0022112067002605](https://doi.org/10.1017/S0022112067002605).
- [2] P. A. Madsen, R. Murray, O. R. Sørensen, A new form of the Boussinesq equations with improved linear dispersion characteristics, *Coastal Engineering* 15 (4) (1991) 371–388. [doi:10.1016/0378-3839\(91\)90017-B](https://doi.org/10.1016/0378-3839(91)90017-B).
- [3] S. Beji, K. Nadaoka, A formal derivation and numerical modelling of the improved boussinesq equations for varying depth, *Ocean Engineering* 23 (8) (1996) 691–704. [doi:\[https://doi.org/10.1016/0029-8018\\(96\\)84408-8\]\(https://doi.org/10.1016/0029-8018\(96\)84408-8\)](https://doi.org/10.1016/0029-8018(96)84408-8).

- [4] O. Nwogu, Alternative form of boussinesq equations for nearshore wave propagation, *Journal of Waterway, Port, Coastal, and Ocean Engineering* 119 (6) (1993) 618–638. [doi:10.1061/\(ASCE\)0733-950X\(1993\)119:6\(618\).1](https://doi.org/10.1061/(ASCE)0733-950X(1993)119:6(618).1).
- [5] P. L.-F. Liu, Model equations for wave propagations from deep to shallow water, *Advances In Coastal And Ocean Engineering: (Volume 1)* (1995) 125–157 [doi:10.1142/9789812797582\\_0003](https://doi.org/10.1142/9789812797582_0003).
- [6] G. Wei, J. T. Kirby, S. T. Grilli, R. Subramanya, A fully nonlinear Boussinesq model for surface waves. Part 1. Highly nonlinear unsteady waves, *Journal of Fluid Mechanics* 294 (1995) 71–92. [doi:10.1017/S0022112095002813](https://doi.org/10.1017/S0022112095002813).
- [7] A. G. Filippini, S. Bellec, M. Colin, M. Ricchiuto, On the nonlinear behaviour of Boussinesq type models: Amplitude-velocity vs amplitude-flux forms, *Coastal Engineering* 99 (2015) 109–123. [doi:10.1016/j.coastaleng.2015.02.003](https://doi.org/10.1016/j.coastaleng.2015.02.003).
- [8] P. J. Lynett, T.-R. Wu, P. L.-F. Liu, Modeling wave runup with depth-integrated equations, *Coastal Engineering* 46 (2) (2002) 89–107. [doi:10.1016/S0378-3839\(02\)00043-1](https://doi.org/10.1016/S0378-3839(02)00043-1).
- [9] K. Sitanggang, P. Lynett, Parallel computation of a highly nonlinear boussinesq equation model through domain decomposition, *International Journal for Numerical Methods in Fluids* 49 (1) (2005) 57–74. [doi:10.1002/fld.985](https://doi.org/10.1002/fld.985).
- [10] F. Shi, J. T. Kirby, J. C. Harris, J. D. Geiman, S. T. Grilli, A high-order adaptive time-stepping TVD solver for Boussinesq modeling of breaking waves and coastal inundation, *Ocean Modelling* 43–44 (2012) 36–51. [doi:https://doi.org/10.1016/j.ocemod.2011.12.004](https://doi.org/10.1016/j.ocemod.2011.12.004).
- [11] M. F. Gobbi, J. T. Kirby, G. Wei, A fully nonlinear boussinesq model for surface waves. part 2. extension to  $o(kh)^4$ , *Journal of Fluid Mechanics* 405 (2000) 181–210. [doi:10.1017/S0022112099007247](https://doi.org/10.1017/S0022112099007247).
- [12] M. Broccchini, A reasoned overview on Boussinesq-type models: the interplay between physics, mathematics and numerics, *Proceedings of the Royal Society A: Mathematical, Physical and Engineering Sciences* 469 (2013) 1–27. [doi:10.1098/rspa.2013.0496](https://doi.org/10.1098/rspa.2013.0496).
- [13] A. E. Green, P. M. Naghdi, A derivation of equations for wave propagation in water of variable depth, *Journal of Fluid Mechanics* 78 (2) (1976) 237–246. [doi:10.1017/S0022112076002425](https://doi.org/10.1017/S0022112076002425).
- [14] P. G. Drazin, R. Johnson, Solitons: an introduction, 2nd edition, Cambridge University Press (1989). [doi:10.1017/CBO9781139172059](https://doi.org/10.1017/CBO9781139172059).
- [15] L. Alzaleq, V. Manoranjan, B. Alzalg, Exact traveling waves of a generalized scale-invariant analogue of the korteweg–de vries equation, *Mathematics* 10 (3) (2022) 414. [doi:10.3390/math10030414](https://doi.org/10.3390/math10030414).
- [16] D.-J. Zhang, S.-L. Zhao, Y.-Y. Sun, J. Zhou, Solutions to the modified korteweg–de vries equation, *Reviews in Mathematical Physics* 26 (07) (2014) 1430006. [doi:10.1142/S0129055X14300064](https://doi.org/10.1142/S0129055X14300064).
- [17] H. Durur, O. Tasbozan, A. Kurt, New analytical solutions of conformable time fractional bad and good modified boussinesq equations, *Applied Mathematics and Nonlinear Sciences* 5 (1) (2020) 447–454. [doi:10.2478/amns.2020.1.00042](https://doi.org/10.2478/amns.2020.1.00042).
- [18] P. J. Lynett, P. L.-F. Liu, Linear analysis of the multi-layer model, *Coastal Engineering* 51 (5-6) (2004) 439–454. [doi:10.1016/j.coastaleng.2004.05.004](https://doi.org/10.1016/j.coastaleng.2004.05.004).
- [19] P. Lynett, P. L.-F. Liu, A two-layer approach to wave modelling, *Proceedings of the Royal Society A: Mathematical, Physical and Engineering Sciences* 460 (2004) 2637–2669. [doi:10.1098/rspa.2004.1305](https://doi.org/10.1098/rspa.2004.1305).
- [20] Z. T. Yang, P. L.-F. Liu, Depth-integrated wave-current models. Part 1. Two-dimensional formulation and applications, *Journal of Fluid Mechanics* 883 (2020) A4. [doi:10.1017/jfm.2019.831](https://doi.org/10.1017/jfm.2019.831).
- [21] Z. T. Yang, P. L.-F. Liu, Depth-integrated wave-current models. Part 2. Currents with an arbitrary profile, *Journal of Fluid Mechanics* 936 (2022) A31. [doi:10.1017/jfm.2022.42](https://doi.org/10.1017/jfm.2022.42).
- [22] K. Parnell, N. Delpeche, I. Didenkulova, T. Dolphin, A. Erm, A. Kask, L. Kelpšaitė, D. Kurenay, E. Quak, A. Räämet, T. Soomere, A. Terentjeva, T. Torsvik, I. Zaitseva-Pärnaste, Far-field vessel wakes in tallinn bay, *Estonian Journal of Engineering* 14 (4) (2008) 273–302. [doi:10.3176/eng.2008.4.01](https://doi.org/10.3176/eng.2008.4.01).
- [23] T. Jiang, R. Henn, S. D. Sharma, Wash waves generated by ships moving on fairways of varying topography, *24th Symposium on Naval Hydrodynamics* (2002) 441–457.
- [24] K. Hirayama, N. Higuchi, A flux source method for ship wave generation in a boussinesq-type wave model, *International Journal of Offshore and Polar Engineering* 30 (3) (2020) 308–317. [doi:10.17736/ijope.2020.008467](https://doi.org/10.17736/ijope.2020.008467).
- [25] M. Do Nascimento, C. Neves, G. De Freitas Maciel, Propagation of ship waves on a sloping bottom, *Proceedings of the Coastal Engineering Conference* (2009) 696–708 [doi:10.1142/9789814277426\\_0059](https://doi.org/10.1142/9789814277426_0059).
- [26] P. L.-F. Liu, T.-R. Wu, Waves generated by moving pressure disturbances in rectangular and trapezoidal channels, *Journal of Hydraulic Research* 42 (2) (2004) 163–171. [doi:10.1080/00221686.2004.9628301](https://doi.org/10.1080/00221686.2004.9628301).
- [27] D. Bayraktar Ersan, S. Beji, Numerical simulation of waves generated by a moving pressure field, *Ocean Engineering* 59 (2013) 231–239. [doi:10.1016/j.oceaneng.2012.12.025](https://doi.org/10.1016/j.oceaneng.2012.12.025).
- [28] C. David, V. Roeber, N. Goseberg, T. Schlurmann, Generation and propagation of ship-borne waves - Solutions from a Boussinesq-type model, *Coastal Engineering* 127 (2017) 170–187. [doi:10.1016/j.coastaleng.2017.07.001](https://doi.org/10.1016/j.coastaleng.2017.07.001).
- [29] M. F. Nascimento, C. F. Neves, G. d. F. Maciel, Waves generated by two or more ships in a channel, *Coastal Engineering Proceedings* 1 (32) (2011) waves.60. [doi:10.9753/icce.v32.waves.60](https://doi.org/10.9753/icce.v32.waves.60).
- [30] F. Shi, M. Malej, J. M. Smith, J. T. Kirby, Breaking of ship bores in a Boussinesq-type ship-wake model, *Coastal Engineering* 132 (2018) 1–12. [doi:10.1016/j.coastaleng.2017.11.002](https://doi.org/10.1016/j.coastaleng.2017.11.002).
- [31] R. C. Ertekin, W. C. Webster, J. V. Wehausen, Waves caused by a moving disturbance in a shallow channel of finite width, *Journal of Fluid Mechanics* 169 (1986) 275–292. [doi:10.1017/S0022112086000630](https://doi.org/10.1017/S0022112086000630).
- [32] T. Torsvik, T. Soomere, Simulation of patterns of wakes from high-speed ferries in Tallinn Bay, *Estonian Journal of Engineering* 57 (3) (2008) 232. [doi:10.3176/eng.2008.3.04](https://doi.org/10.3176/eng.2008.3.04).
- [33] T. Torsvik, I. Didenkulova, T. Soomere, K. E. Parnell, Variability in spatial patterns of long nonlinear waves from fast ferries in Tallinn Bay, *Non-linear Processes in Geophysics* 16 (2) (2009) 351–363.
- [34] P. J. Lynett, P. L.-F. Liu, I. J. Losada, C. Vidal, Solitary Wave Interaction with Porous Breakwaters, *Journal of Waterway, Port, Coastal, and Ocean Engineering* 126 (6) (2000) 314–322. [doi:10.1016/S0733-950X\(00\)126:6\(314\).1](https://doi.org/10.1016/S0733-950X(00)126:6(314).1).
- [35] S. Agarwal, V. Sriram, K. Murali, Modelling wave interaction with porous structures using boussinesq equations, in: *Proceedings of the Fourth International Conference in Ocean Engineering (ICOE2018)*, Springer Singapore, 2019, pp. 573–583.
- [36] D. Ambrosi, L. Quartapelle, A taylor-galerkin method for simulating nonlinear dispersive water waves, *Journal of Computational Physics* 146 (2) (1998) 546–569. [doi:10.1006/jcph.1998.6027](https://doi.org/10.1006/jcph.1998.6027).
- [37] M. Walkley, M. Berzins, A finite element method for the two-dimensional extended Boussinesq equations, *International Journal for Numerical Methods in Fluids* 39 (10) (2002) 865–885. [doi:10.1002/fld.349](https://doi.org/10.1002/fld.349).
- [38] Y. Li, S. Liu, Y. Yu, G. Lai, Numerical modeling of boussinesq equations by finite element method, *Coastal Engineering* 37 (2) (1999) 97–122. [doi:10.1016/S0378-3839\(99\)00014-9](https://doi.org/10.1016/S0378-3839(99)00014-9).
- [39] O. R. Sørensen, H. A. Schäffer, L. S. Sørensen, Boussinesq-type modelling using an unstructured finite element technique, *Coastal Engineering* 50 (4) (2004) 181–198. [doi:10.1016/j.coastaleng.2003.10.005](https://doi.org/10.1016/j.coastaleng.2003.10.005).
- [40] S. B. Woo, P. L.-F. Liu, A Petrov-Galerkin finite element model for one-dimensional fully non-linear and weakly dispersive wave propagation, *International Journal for Numerical Methods in Fluids* 37 (5) (2001) 541–575. [doi:10.1002/fld.186](https://doi.org/10.1002/fld.186).
- [41] S.-B. Woo, P. L.-F. Liu, Finite-Element Model for Modified Boussinesq Equations. I: Model Development, *Journal of Waterway, Port, Coastal, and Ocean Engineering* 130 (1) (2004) 1–16. [doi:10.1016/S0733-950X\(04\)130:1\(1\).1](https://doi.org/10.1016/S0733-950X(04)130:1(1).1).
- [42] C. Eskilsson, S. J. Sherwin, Spectral/hp discontinuous galerkin methods for modelling 2d boussinesq equations, *Journal of Computational Physics* 212 (2) (2006) 566–589. [doi:10.1016/j.jcp.2005.07.017](https://doi.org/10.1016/j.jcp.2005.07.017).
- [43] P. A. Madsen, O. R. Sørensen, A new form of the Boussinesq equations with improved linear dispersion characteristics. Part 2. A slowly-varying bathymetry, *Coastal Engineering* 18 (3-4) (1992) 183–204. [doi:10.1016/0378-3839\(92\)90019-Q](https://doi.org/10.1016/0378-3839(92)90019-Q).
- [44] A. P. Engsig-Karup, J. S. Hesthaven, H. B. Bingham, T. Warburton, DG-FEM solution for nonlinear wave-structure interaction using Boussinesq-type equations, *Coastal Engineering* 55 (3) (2008) 197–208. [doi:10.1016/j.coastaleng.2007.09.005](https://doi.org/10.1016/j.coastaleng.2007.09.005).
- [45] P. A. Madsen, H. B. Bingham, H. Liu, A new Boussinesq method for fully nonlinear waves from shallow to deep water, *Journal of Fluid Mechanics* 462 (2002) 1–30. [doi:10.1017/S0022112002008467](https://doi.org/10.1017/S0022112002008467).

- [46] R. W. Whalin, Wave Refraction Theory in a Convergence Zone, Coastal Engineering (1971) 451–470. [doi:10.9753/icce.v12.139](https://doi.org/10.9753/icce.v12.139).
- [47] T. Dyakonova, A. Khoperskov, Bottom friction models for shallow water equations: Manning's roughness coefficient and small-scale bottom heterogeneity, Journal of Physics: Conference Series 973 (1) (2018) 012032. [doi:10.1088/1742-6596/973/1/012032](https://doi.org/10.1088/1742-6596/973/1/012032).
- [48] O. C. Zienkiewicz, R. L. Taylor, The Finite Element Method for Fluid Dynamics, 5th Edition, Vol. 3, Elsevier, 2014. [doi:10.1016/C2009-0-26328-8](https://doi.org/10.1016/C2009-0-26328-8).
- [49] Wolfram Research, Inc., **Mathematica, Version 12.2**, Champaign, IL (2020).  
URL <https://www.wolfram.com/mathematica>
- [50] M. Ricchiuto, A. Filippini, Upwind residual discretization of enhanced Boussinesq equations for wave propagation over complex bathymetries, Journal of Computational Physics 271 (2014) 306–341. [doi:10.1016/j.jcp.2013.12.048](https://doi.org/10.1016/j.jcp.2013.12.048).
- [51] P. Madsen, O. Sørensen, Bound waves and triad interactions in shallow water, Ocean Engineering 20 (4) (1993) 359–388. [doi:10.1016/0029-8018\(93\)90002-Y](https://doi.org/10.1016/0029-8018(93)90002-Y).
- [52] M. Israeli, S. A. Orszag, Approximation of radiation boundary conditions, Journal of Computational Physics 41 (1) (1981) 115–135. [doi:https://doi.org/10.1016/0021-9991\(81\)90082-6](https://doi.org/10.1016/0021-9991(81)90082-6).
- [53] P. Lancaster, K. Salkauskas, Surfaces generated by moving least squares methods, Mathematics of Computation 37 (1981) 141–158. [doi:10.1090/S0025-5718-1981-0616367-1](https://doi.org/10.1090/S0025-5718-1981-0616367-1).
- [54] J. Orszaghova, A. G. Borthwick, P. H. Taylor, From the paddle to the beach - A Boussinesq shallow water numerical wave tank based on Madsen and Sørensen equations, Journal of Computational Physics 231 (2) (2012) 328–344. [doi:10.1016/j.jcp.2011.08.028](https://doi.org/10.1016/j.jcp.2011.08.028).
- [55] M. Narayanaswamy, A. J. C. Crespo, M. Gómez-Gesteira, R. A. Dalrymple, SPHysics-FUNWAVE hybrid model for coastal wave propagation, Journal of Hydraulic Research 48 (2010) 85–93. [doi:10.1080/00221686.2010.9641249](https://doi.org/10.1080/00221686.2010.9641249).
- [56] M. Tonelli, M. Petti, Hybrid finite volume - finite difference scheme for 2DH improved Boussinesq equations, Coastal Engineering 56 (5-6) (2009) 609–620. [doi:10.1016/j.coastaleng.2009.01.001](https://doi.org/10.1016/j.coastaleng.2009.01.001).
- [57] F. M. White, Fluid Mechanics, 7th Edition, McGraw-Hill, New York, 2010.
- [58] T. H. Havelock, The propagation of groups of waves in dispersive media, with application to waves on water produced by a travelling disturbance, Proceedings of the Royal Society of London A: Mathematical, Physical and Engineering Sciences 81 (549) (1908) 398–430. [doi:10.1098/rspa.1908.0097](https://doi.org/10.1098/rspa.1908.0097).
- [59] T. Soomere, Fast ferry traffic as a qualitatively new forcing factor of environmental processes in non-tidal sea areas: A case study in tallinn bay, baltic sea, Environmental Fluid Mechanics 5 (4) (2005) 293–323. [doi:10.1007/s10652-005-5226-1](https://doi.org/10.1007/s10652-005-5226-1).
- [60] I. Didenkulova, A. Rodin, A typical wave wake from high-speed vessels: Its group structure and run-up, Nonlinear Processes in Geophysics 20 (1) (2013) 179–188. [doi:10.5194/npg-20-179-2013](https://doi.org/10.5194/npg-20-179-2013).
- [61] T. Torsvik, T. Soomere, I. Didenkulova, A. Sheremet, Identification of ship wake structures by a time-frequency method, Journal of Fluid Mechanics 765 (2015) 229–251. [doi:10.1017/jfm.2014.734](https://doi.org/10.1017/jfm.2014.734).

## Appendix A. Analytical integration of FEM terms

The procedure for the analytical integration of the FEM terms using Mathematica software [49] is described below. Consider the integral in  $D_{[3 \times 3]}$  matrix. Given that the Jacobian of a triangular element is denoted as  $J = \begin{bmatrix} J_1 & J_2 \\ J_3 & J_4 \end{bmatrix}$  the expression for the integral with derivatives over a natural triangular element are

expressed as

$$\int_{\Omega} \left[ \frac{\partial \psi_i}{\partial x} h \frac{\partial \psi_j}{\partial x} \right]_{3 \times 3} d\Omega = \frac{|J|}{2} \int_{\xi=0}^{\xi=1} \int_{\gamma=0}^{\gamma=1-\xi} [K] d\gamma d\xi \quad (\text{A.1a})$$

$$[K] = \begin{bmatrix} K_{11} & K_{12} & K_{13} \\ K_{12} & K_{22} & K_{23} \\ K_{13} & K_{23} & K_{33} \end{bmatrix} \quad (\text{A.1b})$$

$$K_{11} = (J_1 + J_2)^2(h_1(-\gamma - \xi + 1) + h_2\xi + \gamma h_3) \quad (\text{A.1c})$$

$$K_{12} = J_1(J_1 + J_2)(h_1(\gamma + \xi - 1) - h_2\xi - \gamma h_3) \quad (\text{A.1d})$$

$$K_{13} = J_2(J_1 + J_2)(h_1(\gamma + \xi - 1) - h_2\xi - \gamma h_3) \quad (\text{A.1e})$$

$$K_{22} = J_1^2(h_1(-\gamma - \xi + 1) + h_2\xi + \gamma h_3) \quad (\text{A.1f})$$

$$K_{23} = J_1 J_2(h_1(-\gamma - \xi + 1) + h_2\xi + \gamma h_3) \quad (\text{A.1g})$$

$$K_{33} = J_2^2(h_1(-\gamma - \xi + 1) + h_2\xi + \gamma h_3) \quad (\text{A.1h})$$

Here  $\xi$  and  $\gamma$  represent the axes in the coordinate system for the natural triangular element and  $h_1, h_2, h_3$  are the nodal values for  $h$ . The analytical integration will result in

$$\int_{\Omega} \left[ \frac{\partial \psi_i}{\partial x} h \frac{\partial \psi_j}{\partial x} \right]_{3 \times 3} d\Omega = \begin{bmatrix} \frac{1}{6}(J_1+J_2)^2(h_1+h_2+h_3) & -\frac{1}{6}J_1(J_1+J_2)(h_1+h_2+h_3) & -\frac{1}{6}J_2(J_1+J_2)(h_1+h_2+h_3) \\ -\frac{1}{6}J_1(J_1+J_2)(h_1+h_2+h_3) & \frac{1}{6}J_1^2(h_1+h_2+h_3) & \frac{1}{6}J_1 J_2(h_1+h_2+h_3) \\ -\frac{1}{6}J_2(J_1+J_2)(h_1+h_2+h_3) & \frac{1}{6}J_1 J_2(h_1+h_2+h_3) & \frac{1}{6}J_2^2(h_1+h_2+h_3) \end{bmatrix} \quad (\text{A.2})$$

which will be directly coded into the program. This prevents the requirement of Gauss quadrature for calculating the integral. The procedure may seem tedious, however it has to be done just for a few combinations of the integrals such as  $\frac{\partial \psi_i}{\partial x} h \frac{\partial \psi_j}{\partial x}$  and  $\psi_i h \frac{\partial \psi_j}{\partial x}$ . Once coded, it can be reused for various expressions by replacing the scalar  $h$ , and by using  $[J_3 J_4]$  for  $y$  derivative instead of  $[J_1 J_2]$ .

## Appendix B. Expressions for domain and boundary integrals

This section provides the expressions for the matrices in the algebraic form of the governing equations given in Eq. (10a). Here  $\Omega$  is the area integral over a triangular element,  $\Gamma$  is boundary integral over the domain-boundary only for the elements along the domain-boundary and  $(n_x, n_y)$  is the outward unit normal for the domain-boundary side.

Mass matrices for each triangular element

$$M_{1[6 \times 6]} = \int_{\Omega} \phi_i \phi_j d\Omega \quad (\text{B.1a})$$

$$M_{2[3 \times 3]} = \int_{\Omega} \psi_i \psi_j d\Omega \quad (\text{B.1b})$$

Matrices in auxiliary variable equation Eq. (10a)

$$D_{[3 \times 3]} = - \int_{\Omega} \left( \frac{\partial \psi_i}{\partial x} h \frac{\partial \psi_j}{\partial x} + \frac{\partial \psi_i}{\partial y} h \frac{\partial \psi_j}{\partial y} \right) d\Omega + \int_{\Gamma} \left( \psi_i h \frac{\partial \psi_j}{\partial x} n_x + \psi_i h \frac{\partial \psi_j}{\partial y} n_y \right) d\Gamma \quad (\text{B.2})$$

Velocity flux gradient matrices in the continuity equation Eq. (10b)

$$C_{x[3 \times 6]} = - \int_{\Omega} \psi_i \frac{\partial \phi_j}{\partial x} d\Omega \quad (\text{B.3a})$$

$$C_{y[3 \times 6]} = - \int_{\Omega} \psi_i \frac{\partial \phi_j}{\partial y} d\Omega \quad (\text{B.3b})$$

Boussinesq terms in the momentum governing equation Eq. (10c)

$$\begin{aligned} B_{1[6 \times 6]} &= \int_{\Omega} \left[ \left( B + \frac{1}{3} \right) \frac{\partial \phi_i}{\partial x} h^2 \frac{\partial \phi_j}{\partial x} \right] d\Omega \\ &\quad + \left[ \left( 2B + \frac{1}{3} \right) \phi_i h \frac{\partial h}{\partial x} \frac{\partial \phi_j}{\partial x} \right] d\Omega \\ &\quad - \int_{\Gamma} \left[ \left( B + \frac{1}{3} \right) \phi_i h^2 \frac{\partial \phi_j}{\partial x} \right] n_x d\Gamma \end{aligned} \quad (\text{B.4a})$$

$$\begin{aligned} B_{2[6 \times 6]} &= \int_{\Omega} \left[ \left( B + \frac{1}{3} \right) \frac{\partial \phi_i}{\partial x} h^2 \frac{\partial \phi_j}{\partial y} \right] d\Omega \\ &\quad + \left[ \left( 2B + \frac{1}{2} \right) \phi_i h \frac{\partial h}{\partial x} \frac{\partial \phi_j}{\partial y} - \frac{1}{6} \phi_i h \frac{\partial h}{\partial y} \frac{\partial \phi_j}{\partial x} \right] d\Omega \\ &\quad - \int_{\Gamma} \left[ \left( B + \frac{1}{3} \right) \phi_i h^2 \frac{\partial \phi_j}{\partial y} \right] n_x d\Gamma \end{aligned} \quad (\text{B.4b})$$

$$\begin{aligned} B_{3[6 \times 6]} &= \int_{\Omega} \left[ \left( B + \frac{1}{3} \right) \frac{\partial \phi_i}{\partial y} h^2 \frac{\partial \phi_j}{\partial x} \right] d\Omega \\ &\quad + \left[ \left( 2B + \frac{1}{2} \right) \phi_i h \frac{\partial h}{\partial y} \frac{\partial \phi_j}{\partial x} - \frac{1}{6} \phi_i h \frac{\partial h}{\partial x} \frac{\partial \phi_j}{\partial y} \right] d\Omega \\ &\quad - \int_{\Gamma} \left[ \left( B + \frac{1}{3} \right) \phi_i h^2 \frac{\partial \phi_j}{\partial x} \right] n_y d\Gamma \end{aligned} \quad (\text{B.4c})$$

$$\begin{aligned} B_{4[6 \times 6]} &= \int_{\Omega} \left[ \left( B + \frac{1}{3} \right) \frac{\partial \phi_i}{\partial y} h^2 \frac{\partial \phi_j}{\partial y} \right] d\Omega \\ &\quad + \left[ \left( 2B + \frac{1}{3} \right) \phi_i h \frac{\partial h}{\partial y} \frac{\partial \phi_j}{\partial y} \right] d\Omega \\ &\quad - \int_{\Gamma} \left[ \left( B + \frac{1}{3} \right) \phi_i h^2 \frac{\partial \phi_j}{\partial y} \right] n_y d\Gamma \end{aligned} \quad (\text{B.4d})$$

$$B_{5[6 \times 3]} = \int_{\Omega} B g \left[ \phi_i h^2 \frac{\partial \psi_j}{\partial x} \right] d\Omega \quad (\text{B.4e})$$

$$B_{6[6 \times 3]} = \int_{\Omega} B g \left[ \phi_i h^2 \frac{\partial \psi_j}{\partial y} \right] d\Omega \quad (\text{B.4f})$$

All of the expression above are independent of time and only require a one-time calculation in the beginning of the simulation. The following matrices are dependant on time and are calculated at each step of the RK4 time-stepping algorithm.

Advection matrices in momentum equations Eq. (10c)

$$\begin{aligned} N_{[6 \times 6]} &= - \int_{\Omega} \left[ \phi_i \left( \frac{P}{d} \right) \frac{\partial \phi_j}{\partial x} + \phi_i \frac{\partial}{\partial x} \left( \frac{P}{d} \right) \phi_j \right] d\Omega \\ &\quad + \left[ \phi_i \left( \frac{Q}{d} \right) \frac{\partial \phi_j}{\partial y} + \phi_i \frac{\partial}{\partial y} \left( \frac{Q}{d} \right) \phi_j \right] d\Omega \end{aligned} \quad (\text{B.5})$$

Elevation gradient matrices in momentum equations Eq. (10c)

$$G_{x[6 \times 3]} = - \int_{\Omega} g \left[ \phi_i d \frac{\partial \psi_j}{\partial x} \right] d\Omega \quad (\text{B.6a})$$

$$G_{y[6 \times 3]} = - \int_{\Omega} g \left[ \phi_i d \frac{\partial \psi_j}{\partial y} \right] d\Omega \quad (\text{B.6b})$$

Surface-pressure gradient matrices in momentum equations Eq. (10c)

$$E_{x[6 \times 6]} = - \int_{\Omega} \frac{1}{\rho} \left[ \phi_i d \frac{\partial \phi_j}{\partial x} \right] d\Omega \quad (\text{B.7a})$$

$$E_{y[6 \times 6]} = - \int_{\Omega} \frac{1}{\rho} \left[ \phi_i d \frac{\partial \phi_j}{\partial y} \right] d\Omega \quad (\text{B.7b})$$

## Appendix C. Dispersion error in the mixed numerical scheme

The work in [50] reported the dispersion error as a function of the mesh-size for various numerical schemes applied to the 1DH Madsen and Sørensen's equations [43]. This section briefly reports numerically evaluated dispersion error for the mixed numerical scheme of FEBOUSS, where the basis function is linear for  $\eta$  and quadratic polynomial for  $P$  and  $Q$ . The dispersion error in this study is represented as the relative difference between numerical and analytical wave-celerity. Simulations were carried out for a regular wave with time-period  $T = 1.25$ s, wave-height  $H = 0.02$ m in water-depth  $h = 1$ m corresponding to wave-length  $L = 2.41$ m and  $kh = 2.6$ . Table C.4 lists the various mesh-sizes, where  $N = L/\Delta x$  is the number of elements along a single wave-length. The numerical wave-celerity  $C$  was calculated using  $\eta$  time-series at two wave-probes and compared against the analytical celerity  $C_{MS}$  from [43] given by the following expression with  $B = 1/15$ .

$$C_{MS}^2 = gh \frac{1 + Bk^2h^2}{1 + (B + 1/3)k^2h^2} \quad (\text{C.1})$$

$C_{MS} = 1.9798 \text{ m s}^{-1}$  for the tested regular wave. Fig. (C.30) presents the quadratic trend of the dispersion error for the FEBOUSS scheme through a plot of relative error in wave-celerity against the mesh-size.

## Appendix D. Estimation of wave-length at the cusps

The analytical expressions for half-wedge angle  $\theta_K$  and corresponding wave-length at cusps  $L_H$  were derived in [58] for point disturbance moving at a constant speed in still water at finite depths. We take  $h$  as still water-depth,  $k = 2\pi/L_H$  as the wavenumber and  $V_s$  as the speed of the moving disturbance.

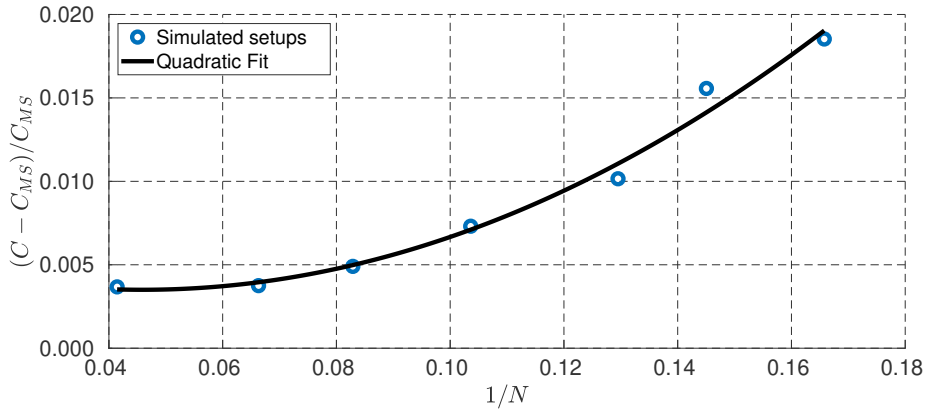


Figure C.30: Relative error in numerical value of wave-crelarity  $C$  compared against analytical value  $C_{MS}$  for a regular wave with  $kh = 2.6$ . Here,  $N$  is the number of elements along a single wave-length.

Table C.4: Details for mesh setup for simulating regular wave with  $kh = 2.6$ . Here,  $N$  is the number of elements per wave-length.

SN	$N$	$1/N$	Celerity $C$	Relative Error $\frac{C-C_{MS}}{C_{MS}}$
1	24.13	0.0414	1.9870	0.0037
2	15.08	0.0663	1.9872	0.0037
3	12.06	0.0829	1.9895	0.0049
4	9.65	0.1036	1.9942	0.0073
5	7.72	0.1295	1.9999	0.0102
6	6.89	0.1450	2.0106	0.0156
7	6.03	0.1658	2.0164	0.0185

The depth Froude number is given by  $Fr_d = V_s / \sqrt{gh}$ . The coefficients  $p$ ,  $m$  and  $n$  as defined in [58] are given below. For finite depths, both  $m$  and  $n$  are dependant on  $k$  and have a lower and upper limit of 0 and 1.

$$p = \frac{1}{Fr_d^2} = \frac{gh}{V_s^2}, \quad m = \frac{\tanh kh}{kh}, \quad n = \frac{2kh}{\sinh 2kh} \quad (\text{D.1})$$

a) *Sub-critical range*  $Fr_d < 1$ . The sub-critical range consists of both the transverse and the divergent wave systems, with the line of cusps at the crossing between the two systems. The wave-length at cusps is obtained through iterative solution of following equation

$$m(3-n) = \frac{2}{p} \quad \Rightarrow \quad \frac{\tanh kh}{kh} \left( 3 - \frac{2kh}{\sinh 2kh} \right) = \frac{2gh}{V_s^2}, \quad (\text{D.2})$$

where  $k$  is the only unknown. Using the obtained value of  $k$ , the half-wedge angle  $\theta_K$  is given by

$$\theta_K = \cos^{-1} \left( \frac{\sqrt{8(1-n)}}{(3-n)} \right). \quad (\text{D.3})$$

With the increasing  $Fr_d$ , the value of  $\theta_K$  increases, while the divergent system becomes more dominant compared to the transverse wave system. The critical value of  $Fr_d = 1$  has the maximum  $\theta_K = 90^\circ$ .

The example in section 4.3 is for a disturbance moving at a speed of  $V_s = 5.95 \text{ m s}^{-1}$  at a depth of  $h = 5 \text{ m}$ , corresponding to a sub-critical depth Froude number  $Fr_d = 0.85$ . By solving Eq. (D.2) iteratively, we get the value of  $k = 0.3717 \text{ m}^{-1}$ , corresponding to  $L_H = 16.9052 \text{ m}$ ,  $n = 0.1808$ , resulting in  $\theta_K = 24.76^\circ$  using Eq. (D.3).

b) *Super-critical range*  $Fr_d > 1$ . The super-critical range consists only of the divergent wave system, while the transverse system and the line of cusps disappear. The half-wedge angle is given by

$$\theta_K = \sin^{-1}(\sqrt{p}). \quad (\text{D.4})$$

With increasing  $Fr_d$ , the value of  $\theta_K$  reduces.